COMENIUS UNIVERSITY IN BRATISLAVA
FACULTY OF MATHEMATICS, PHYSICS
AND INFORMATICS

Ion Channel Degeneracy: On Function-Energy Trade-Offs in a Canonical CA1 Pyramidal Cell Model

Diploma Thesis

2026 Marvin Marz

COMENIUS UNIVERSITY IN BRATISLAVA
FACULTY OF MATHEMATICS, PHYSICS
AND INFORMATICS

Ion Channel Degeneracy: On Function-Energy Trade-Offs in a Canonical CA1 Pyramidal Cell Model

Diploma Thesis

Study program: Cognitive Science
Field of study: 2503, Cognitive Science
Supervising department: Department of Applied Informatics
Supervisor(s): Mgr. Matúš Tomko, PhD.; Prof. MUDr. Peter Jedlička, PhD.

2026 Marvin Marz

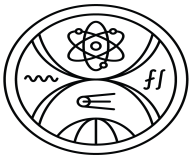

Univerzita Komenského v Bratislave
Fakulta matematiky, fyziky a informatiky

PRIHLÁŠKA NA ZÁVEREČNÚ PRÁCU

Meno a priezvisko študenta: Marvin Steven Marz
Študijný program: kognitívna veda (Jednoodborové štúdium, magisterský II. st., denná forma)
Študijný odbor: 18. - informatika
Typ záverečnej práce: diplomová
Jazyk záverečnej práce: anglický
Sekundárny jazyk: slovenský

Názov: Ion Channel Degeneracy: On Function-Energy Trade-Offs in a Canonical CA1 Pyramidal Cell Model

Anotácia: Ion channel degeneracy is defined as a many-to-one functional relationship in which different combinations of ion channels give rise to similar functional or electrophysiological properties. The parameter space of the model will be explored and compared with the functional space. Principles of Pareto optimality will be used to elucidate potential functional-energetic trade-offs in hippocampal CA1 pyramidal cells.

Cieľ: Evaluate ion channel degeneracy in hippocampal CA1 pyramidal cells by using a biophysically constrained evolutionary search to identify functionally valid parameter combinations and explore functional-energetic trade-offs.

Literatúra:
Goaillard, J.-M., & Marder, E. (2021). Ion Channel Degeneracy, Variability, and Covariation in Neuron and Circuit Resilience. Annual Review of Neuroscience, 44(1), 335–357.
Jedlicka, P., Bird, A. D., & Cuntz, H. (2022). Pareto optimality, economy–effectiveness trade-offs and ion channel degeneracy: Improving population modelling for single neurons. Open Biology, 12(7), 220073.
Roy, A., & Narayanan, R. (2021). Spatial information transfer in hippocampal place cells depends on trial-to-trial variability, symmetry of place-field firing, and biophysical heterogeneities. Neural Networks, 142, 636–660.

Vedúci: Mgr. Matúš Tomko, PhD.
Konzultant: prof. MUDr. Peter Jedlička, PhD.
Katedra: FMFI.KAI - Katedra aplikovanej informatiky
Vedúci katedry: doc. RNDr. Tatiana Jajcayová, PhD.

Dátum schválenia: 28.01.2025

podpis študenta

Comenius University Bratislava
Faculty of Mathematics, Physics and Informatics

THESIS ASSIGNMENT

Name and Surname: Marvin Steven Marz
Study programme: Cognitive Science (Single degree study, master II. deg., full time form)
Field of Study: Computer Science
Type of Thesis: Diploma Thesis
Language of Thesis: English
Secondary language: Slovak

Title: Ion Channel Degeneracy: On Function-Energy Trade-Offs in a Canonical CA1 Pyramidal Cell Model

Annotation: Ion channel degeneracy is defined as a many-to-one functional relationship in which different combinations of ion channels give rise to similar functional or electrophysiological properties. The parameter space of the model will be explored and compared with the functional space. Principles of Pareto optimality will be used to elucidate potential functional-energetic trade-offs in hippocampal CA1 pyramidal cells.

Aim: Evaluate ion channel degeneracy in hippocampal CA1 pyramidal cells by using a biophysically constrained evolutionary search to identify functionally valid parameter combinations and explore functional-energetic trade-offs.

Literature:
Goaillard, J.-M., & Marder, E. (2021). Ion Channel Degeneracy, Variability, and Covariation in Neuron and Circuit Resilience. Annual Review of Neuroscience, 44(1), 335–357.
Jedlicka, P., Bird, A. D., & Cuntz, H. (2022). Pareto optimality, economy–effectiveness trade-offs and ion channel degeneracy: Improving population modelling for single neurons. Open Biology, 12(7), 220073.
Roy, A., & Narayanan, R. (2021). Spatial information transfer in hippocampal place cells depends on trial-to-trial variability, symmetry of place-field firing, and biophysical heterogeneities. Neural Networks, 142, 636–660.

Supervisor: Mgr. Matúš Tomko, PhD.
Consultant: prof. MUDr. Peter Jedlička, PhD.
Department: FMFI.KAI - Department of Applied Informatics
Head of department: doc. RNDr. Tatiana Jajcayová, PhD.

Assigned: 28.01.2025

Approved: 28.01.2025 prof. Ing. Igor Farkaš, Dr.
Guarantor of Study Programme

Student

Supervisor

Declaration

I hereby declare that the work presented in this thesis is original and the result of my own investigations. Formulations and ideas taken from other sources are cited as such.

. . . . . .

Acknowledgments

I want to thank Mgr. Matúš Tomko and Prof. MUDr. Peter Jedlička for their ongoing support and encouragement. You have inspired me to keep working and sparked my imagination for my future endeavors.

I am also very grateful for Dr. Alexander Bird's advice and assistance. Thank you for sharing your ideas with me and for motivating me to consider new perspectives.

During the preparation of this work, AI tools, including ChatGPT and Grammarly, were used for language refinement, code debugging, and data visualization support. Responsibility for the final form of the text remains with the author.

Abstrakt

Keď sa stretneme s degeneráciou iónových kanálov v nervových bunkách, t. j. so schopnosťou rôznych konštelácií iónových kanálov vyvolávať podobné elektrofyziologické vlastnosti, môžeme si položiť niekoľko otázok. Aké konštelácie rôznych typov iónových kanálov by sa mali uprednostňovať za akých podmienok? Existuje hlavný princíp (alebo princípy), ktorý obmedzuje degeneráciu iónových kanálov? Aký druh funkčných kompromisov možno nájsť v konglomeráte vzťahov mnohých k jednému, ak vôbec nejaké existujú? V tejto práci používame biofyzikálne obmedzenú stratégiu stochastického vyhľadávania na plne morfologickom modeli pyramídovej bunky CA1 hipokampu potkana založenom na vodivosti - zahŕňajúcom desať aktívnych iónových kanálov na posúdenie rôznych parametrických kombinácií funkčne platných modelov. Z tohto dôvodu ukladáme modelu biologicky vierohodné funkčné kritériá, a to priestorové kódovanie (účinnosť) a spotrebu adenozíntrifosfátu (ATP) (energetická účinnosť). Nasadenie týchto cieľov nám umožňuje preskúmať priestor parametrov modelu a porovnať ho s funkčným priestorom našich kritérií. Tým sme schopní potvrdiť degeneráciu iónových kanálov s ohľadom na Paretoovu optimálnosť ako zastrešujúci princíp spoluúčasti iónových kanálov a objasniť potenciálne kompromisy medzi funkciou a energiou v hipokampálnych pyramídových bunkách CA1. Prekvapivo sme nezistili žiadny jasný globálny kompromis medzi energetickou účinnosťou a priestorovým kódovaním, hoci modelová populácia vykazovala výraznú degeneráciu iónových kanálov. Pozorovali sme však vznikajúcu Paretovu frontu, ktorá bola obmedzená našou funkciou zdatnosti.

Kľúčové slová: CA1, pyramídová bunka, hipokampus potkana, degenerácia iónových kanálov, Paretova optimálnosť, stochastická stratégia vyhľadávania, model založený na vodivosti, priestorové kódovanie, energetická účinnosť

Translated with DeepL.com

Abstract

Ion channel degeneracy refers to the phenomenon whereby different combinations of ion channels can produce similar electrophysiological or functional properties. When this degeneracy occurs in cells, several questions emerge. Which combinations of ion channel types should be preferred under specific conditions? Is there a guiding principle—or multiple principles—that limit this degeneracy? What kinds of functional trade-offs, if any, exist within these many-to-one relationships? In this study, we used a biophysically constrained stochastic search method on a full-morphological, conductance-based model of a rat hippocampal CA1 pyramidal cell—covering 22 active and passive intrinsic parameters, including ion channel conductances, distribution slopes, and membrane resistance—to evaluate different parameter combinations to produce functionally valid models. We applied experimentally verified functional criteria to the models, focusing on intrinsic somatodendritic and spatial-coding measures. Next, we calculated spatial information transfer (effectiveness) and adenosine triphosphate (ATP consumption (energy efficiency) during virtual place field traversal. Using these objectives, we explored the population's parameter space and compared it with the functional space defined by our criteria. This approach enabled us to investigate ion channel degeneracy using Pareto optimality as a fundamental principle of ion channel co-expression and to clarify the trade-offs between function and energy demands in hippocampal CA1 pyramidal cells. Surprisingly, we found no clear global trade-off between energy efficiency and spatial coding, even though the model population robustly exhibited ion-channel degeneracy. However, we observed an emerging Pareto front constrained by our fitness function.

Keywords: CA1, pyramidal cell, rat hippocampus, ion channel degeneracy, Pareto optimality, stochastic search strategy, conductance-based model, spatial coding, energy efficiency

Table of Contents

1 Introduction 1

2 Theoretical Background 3

2.1 Ion Channel Degeneracy 4

2.2 Evolutionary Objectives 8

2.3 Pareto Optimality 10

2.4 CA1 Place Cells 13

3 Methods 15

3.1 NEURON 16

3.2 The Base Model 17

3.3 Active Conductances 18

3.4 Synaptic Input 19

3.5 Place-Field Simulation 20

3.6 Output Measures 20

3.7 Information-Theoretic Analysis 22

3.8 Stochastic-Search Procedure 23

3.9 Energy-Theoretic Analysis 26

3.10 Pareto Front Calculation 27

3.11 Computational Details 27

4 Results 28

4.1 Place Cell Properties 28

4.2 Parameter Degeneracy 31

4.3 Information- and Energy-Theoretic Analysis 41

5 Discussion 47

5.1 Biophysical Interpretation 48

5.2 Consequences for Cognitive Science 48

5.3 Implications for Modeling and Experiments 49

5.4 Limitations and Future Directions 50

6 Conclusion 51

7 Literature 52

8 Appendix 59

1 Introduction

In recent years, interest has grown in the phenomenon of ion channel degeneracy and its underlying explanations (Goaillard et al., 2009; Goaillard & Marder, 2021; Jain & Narayanan, 2020; Jedlicka et al., 2022; Marder & Bucher, 2007; Marder & Goaillard, 2006; Mittal & Narayanan, 2022; Rathour & Narayanan, 2014; Roy & Narayanan, 2021; Seenivasan & Narayanan, 2020; Stöber et al., 2023). Ion channel degeneracy is defined as a functional many-to-one relationship in which different combinations of ion channels yield similar functional or electrophysiological characteristics. Despite recent advances in understanding this phenomenon, many questions remain open, such as what constraints affect ion channel degeneracy, whether a guiding principle exists, and if there are functional trade-offs.

Jedlicka et al. (2022) addressed some of these questions in their review paper on Pareto optimality in single neurons. The authors explain that Pareto optimality provides a useful framework for balancing evolutionary trade-offs across multiple tasks. They propose that Pareto optimality could guide efforts to address ion channel degeneracy by identifying subpopulations of conductance-based models that balance efficiency and functionality. A state is considered Pareto optimal if it achieves the best possible trade-off between various criteria, meaning improving one criterion would worsen another. The Pareto front includes all Pareto-optimal configurations. Additionally, the Pareto front provides useful insights into model configurations. The high-dimensional parameter space of neuronal models can be reduced to lower-dimensional manifolds, which might explain experimentally observed ion channel correlations.

Additional work on ion channel degeneracy was carried out by Narayanan (Jain & Narayanan, 2020; Mittal & Narayanan, 2022; Roy & Narayanan, 2021; Seenivasan & Narayanan, 2020). In one study, Roy and Narayanan (2021) used a stochastic search method encompassing thousands of models, employing stimulus-specific information (SSI) and mutual information (MI) metrics at various locations within the place fields of hippocampal place cells to analyze spatial information transfer. They discovered that ion channel degeneracy plays a crucial role in regulating spatial information transfer, alongside trial-to-trial variability and tuning-curve shape. In another study by Jain and Narayanan (2020), the authors demonstrated ion-channel degeneracy in the excitability

and encoding features of hippocampal pyramidal neurons, as evidenced by the spike-triggered average.

Del Giudice and Crespi (2018) introduced a basic framework for functional trade-offs in cognition that applies to both natural and artificial systems. The authors identified fundamental functional properties shared by all systems, such as performance, efficiency, robustness, and flexibility. Many trade-offs can emerge among these properties.

In this thesis, we examined:

(RQ1) To what extent is ion channel degeneracy affected by function-energy trade-offs, and does it demonstrate Pareto-optimal behavior?

(H1) Specifically, we hypothesized that CA1 pyramidal cells exhibit trade-offs between spatial coding effectiveness and energy efficiency, following Pareto-optimal principles.

We employed a stochastic search strategy on a full-morphological, conductance-based CA1 pyramidal cell model of the rat hippocampus. This resulted in valid models that adhere to biophysical constraints derived from intrinsic somatodendritic measurements and exhibit realistic parameter ranges for spatial coding. We computed pairwise correlations of parameters to assess heterogeneity across the entire parameter space. Subsequently, we performed post hoc tests to examine the effects of our two objectives: spatial information transfer, measured as MI, and adenosine triphosphate (ATP) consumption during virtual place-field traversal. Lastly, we used quantitative analysis tools to determine whether Pareto fronts guide the trade-offs among our valid models, represented by a fitness function, and to visualize these trade-offs. This approach provided the necessary tools to address our research question. If no Pareto front with a plausible distribution of valid model configurations is found, this would falsify our hypothesis (confirming H0).

The thesis is organized as follows: In Chapter 2, we present the necessary theoretical background to understand ion-channel degeneracy and Pareto optimality (Sections 2.1 and 2.3). We also introduce the concept of evolutionary objectives (2.2) and provide a functional overview of CA1 pyramidal cells and the task of spatial coding (2.4). In Chapter 3, we describe the methods used in this thesis. Starting with the computational software that forms the foundation of this work (3.1), we then detail the classification of the base model (3.2), the set of active conductances incorporated into the model (3.3), the

structure of the synaptic input (3.4), the place-field simulation (3.5), the output measurements (3.6), the information-theoretic analysis (3.7), the energy-theoretic analysis (3.8), the specific objective ("fitness function") employed to calculate the Pareto front (3.9), the stochastic-search procedure used to generate a population of candidate cells (3.10), and finally, the computational details of the simulation (3.11). In Chapter 4, we present the results of the simulations. The chapter is divided into the following sections: the analysis of intrinsic and functional properties of our final place cell population (4.1), the description of the populations' parameter degeneracy (4.2), and the information- and energy-theoretic analysis. Lastly, in Chapter 5, we discuss the findings through the lens of biophysical implications of ion channel degeneracy (5.1), relate them to the broader context of cognitive sciences (5.2), and modeling in general (5.3). We conclude with a critical reflection on the limitations of this thesis and potential future directions (5.4).

2 Theoretical Background

With the surge of new data in modern neuroscience, an important quest of science is to understand this data and develop theories about it. In recent decades, there has been a boom in neuroscientific theories, such as the efficient coding hypothesis (Barlow, 1961), the temporal binding hypothesis (von der Malsburg, 1981; Damasio, 1989; Singer & Gray, 1995; Engel et al., 2001), the global neuronal workspace theory (Dahaene, 2001), and the integrated information theory (Tononi et al., 2016). Theory and data mutually influence each other, creating new paths for scientific discovery. Therefore, it is crucial to consider both theory and data simultaneously. The upcoming work of in-silico experimentation aims to do exactly that—asking questions grounded in theory and generating data that can support or challenge hypotheses in the Popperian sense. As a result, this chapter will provide an overview of the key theories underlying this work.

We will start by examining the phenomenon of ion channel degeneracy (2.1), then discuss the evolutionary goals behind organism design and the related trade-offs (2.2). Next, we will introduce the concept of optimal trade-offs based on Pareto optimality (2.3) and conclude with a discussion of the role of pyramidal cells in the hippocampal CA1 region (2.4).

2.1 Ion Channel Degeneracy

The idea of degeneracy in biological systems originates from Edelman and Gally, who first described it as:

"[…] the ability of elements that are structurally different to perform the same function or yield the same output" (Edelman & Gally, 2001, p. 13763).

Since then, researchers have used this term to describe solutions that yield similar or nearly identical behaviors (Goaillard & Marder, 2021). Therefore, degeneracy must be distinguished from redundancy, which refers to different copies of systems, such as in engineering, including electrical generators and navigation systems (Marder & Goaillard, 2006). Instead, a system's robustness and flexibility are achieved simultaneously through overlapping functions and compensation (Marder & Goaillard, 2006; Jedlicka et al., 2022; Stöber et al., 2023; Figures 2.1 and 2.2).

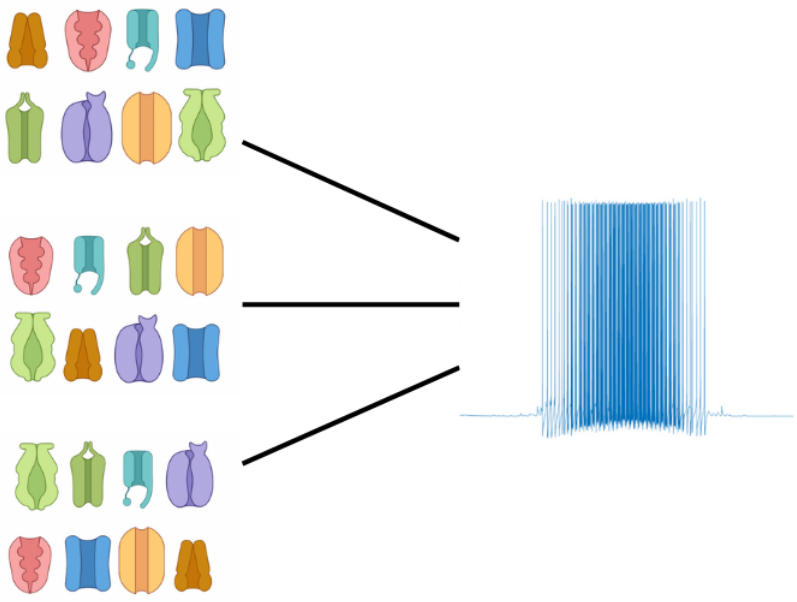

Figure 2.1: Illustration of ion channel degeneracy. Distinct constellations of ion channel arrangements (left side) that produce similar electrophysiological output (right side). The voltage trace on the right has the typical shape of a place field response.

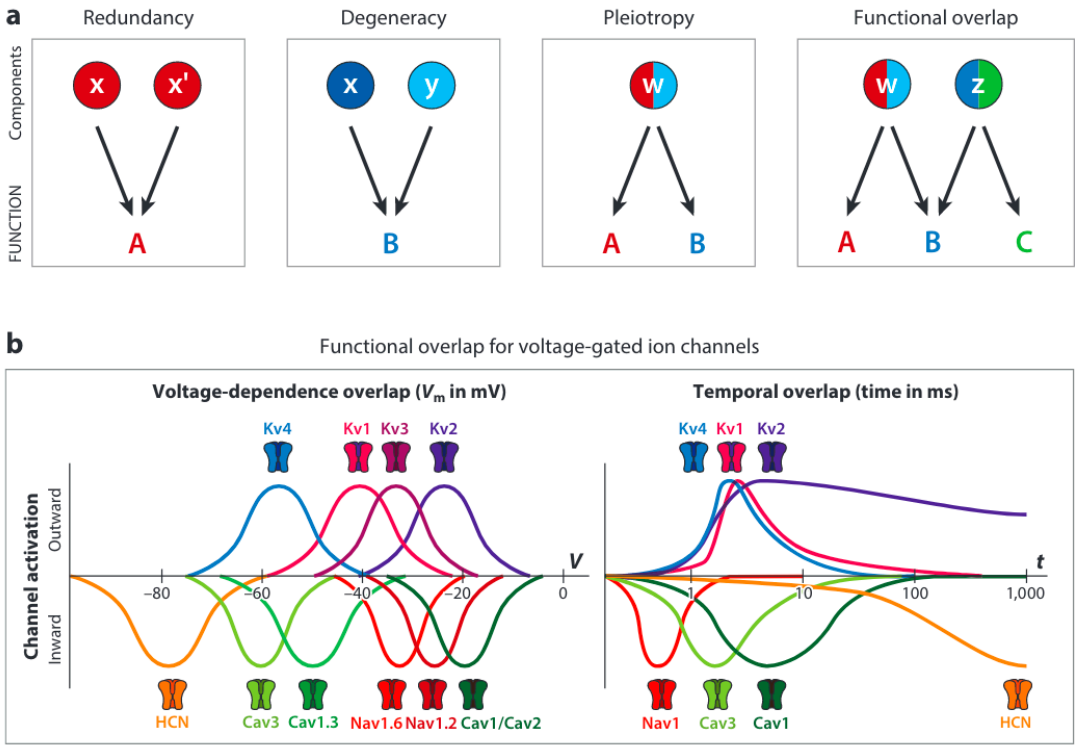

Figure 2.2: Functional Overlap of Ion Channels. (a) Core concepts of redundancy, degeneracy, pleiotropy, and functional overlap. Redundancy involves identical copies of the same component: x and x′ performing the same function (A). Degeneracy involves nonidentical components: x and y performing the same function (B). Pleiotropy or plurifunctionality refers to biological components (w) participating in two or more functional processes (A and B). Functional overlap occurs when two pleiotropic components, w and z, partially degenerate and share a function (B) while maintaining distinct functional roles (A-B versus B-C). (b) Degeneracy and functional overlap of voltage-gated ion channels happen when these channels have overlapping voltage sensitivities and gating kinetics. Families of voltage-gated ion channels are shown with approximate voltage sensitivities. Reproduced from Goaillard and Marder (2021).

The phenomenon gained scientific attention through pioneering work by Eve Marder and others on the stomatogastric nervous system (STN) of crustaceans (Marder & Goaillard, 2006; Marder & Bucher, 2007; Goaillard et al., 2009). Specifically, they studied the stomatogastric ganglion (STG), a cluster of neuron cell bodies outside the central nervous system (CNS). The STG usually contains about 30 neurons, depending on the species used in the experiment, including the motor neurons that control the stomach muscles to aid digestion (Marder & Bucher, 2007). The system functions as a central pattern generator that produces a rhythmic activity pattern known as the pyloric rhythm (Goaillard et al., 2009). The pyloric circuit features a triphasic motor pattern in which the pyloric dilator, lateral pyloric, and pyloric neurons work together to generate

bursts of action potentials that lead to pyloric contractions (Goaillard et al., 2009). Its small size makes this system an excellent model for study. Therefore, using both intracellular and extracellular recordings, researchers can observe the entire system in vitro after dissection (Marder & Bucher, 2007).

Degeneracy is a common feature of biological systems that provides robustness and flexibility, enabling organisms to adapt to constantly changing environments. Variability in ion channel expression can act as a buffer, shielding the system from disturbances in its natural surroundings. For instance, the co-regulation of the hyperpolarization-activated cyclic nucleotide-gated (HCN) channel with the A-type (IA) potassium channel, or with the intermediate-conductance calcium-activated potassium (IK) channel, has a stabilizing effect on specific electrophysiological properties. This is because the opposing currents balance each other as long as their magnitudes vary together (Goaillard & Marder, 2021). Thus, the covariation in channel expression helps stabilize certain firing characteristics rather than hinder them. Consequently, biophysical diversity enhances both robustness and flexibility (Goaillard & Marder, 2021).

Furthermore, degeneracy can lead to unexpected pharmacological results. Drugs and knockout experiments targeting ion channels often do not produce clear changes in the cell's electrophysiological phenotype. This is because compensatory adjustments in ion channel expression and overlapping channels can account for the lack of changes in activity (Goaillard & Marder, 2021). Swensen and Bean (2005) found that sodium and calcium currents in Purkinje neurons exhibit significant cell-to-cell variability, meaning their roles in action potential generation can be substantial or nearly absent. Ultimately, they discovered that different ratios of inward sodium and calcium currents can yield similar voltage responses in various neurons with nearly identical activation profiles (Marder & Goaillard, 2006). Conversely, pharmacological interventions can produce different effects within the same cell type because the outcome depends on the combination of parameters that drives the specific change. For example, changes in the density of HCN channels in pyloric dilator neurons cannot be fully compensated for because the regulatory relationship between HCN and IA channels is non-reciprocal (Marder & Goaillard, 2006). Additionally, studies have shown that a slow, long-term compensatory mechanism can counteract ion channel overexpression to regulate neuronal excitability (Marder & Goaillard, 2006). This demonstrates that:

"[…] slow developmental and homeostatic mechanisms can 'find' multiple solutions of correlated and compensating values of membrane conductances consistent with a given activity pattern, even while rapid pharmacological treatments that vary the values of one current at a time result in altered activity" (Marder & Goaillard, 2006, p. 567).

Theoretical research has consistently shown that different parameter combinations can produce similar phenotypes, indicating a many-to-one relationship between the parameter space and the functional space within a cell type (Alonso & Marder, 2019; Jain & Narayanan, 2020; Mittal & Narayanan, 2022; Rathour & Narayanan, 2014; Roy & Narayanan, 2021). Notably, Rathour and Narayanan (2014) demonstrated the emergence of similar functional maps along the dendritic tree of a group of CA1 pyramidal cells. They propose:

"[…] collective channelostasis, where several channels regulate their properties and expression profiles in an uncorrelated manner, as an alternative for accomplishing homeostasis of functional maps" (Rathour & Narayanan, 2014, p. 1787).

In another study, Roy and Narayanan (2021) conducted a stochastic search across thousands of models, using stimulus-specific and mutual information metrics at different locations within the place fields of hippocampal place cells, to analyze spatial information transfer. They found that ion channel degeneracy plays a key role in regulating spatial information transfer, as well as trial-to-trial variability, and the shape of tuning curves. Additionally, Jain & Narayanan (2020) showed the presence of ion channel degeneracy in the excitability and encoding features of hippocampal pyramidal neurons, as demonstrated in the spike-triggered average (Figure 2.3).

Although degeneracy can occur at various levels of the system, including cellular, network, and system levels, we focus in this thesis on degeneracy related to ion channel manifolds, as previously outlined. Overall, degeneracy is a key feature of:

"[…] biological systems that need to be robust and resilient against perturbations, as smooth transitions between the contributions of different channels can expand the dynamic range of a neuron or circuit." (Goaillard & Marder, 2021, p. 338).

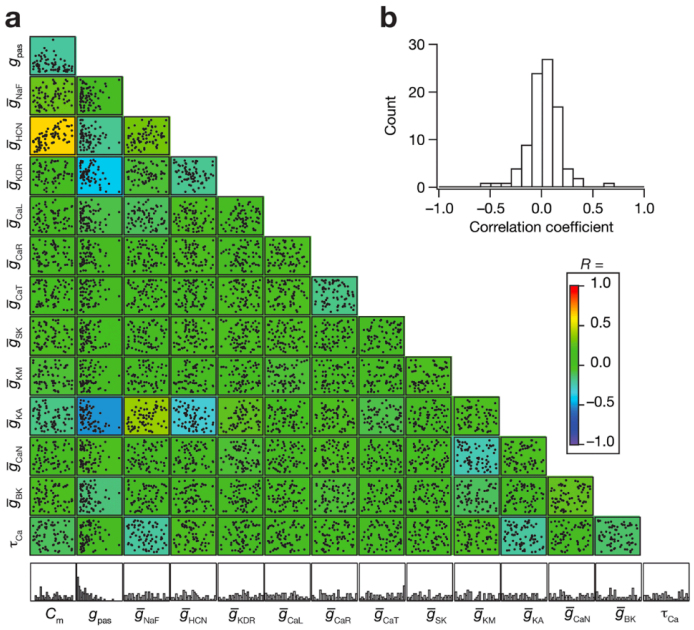

Figure 2.3: Distributions of pairwise correlations of parameters among valid models that simultaneously express excitability and encoding measurements. (a) A correlation matrix showing pairwise relationships between 14 parameters (13 of which are ion channel related) across 72 valid models. Each subplot is a scatter plot showing the values of two parameters, labeled on the bottom and left axes. The bottom row contains normalized histograms of the 14 parameters across all 72 models, showing a broad distribution spanning the entire parametric range. These plots are overlaid on the lower diagonal of a color-coded matrix of Pearson correlation coefficients. (b) Histogram of the correlation coefficients derived from the scatter plots in panel a. Reproduced from Jain and Narayanan (2020).

2.2 Evolutionary Objectives

Evolution can rightly be seen as the primary force behind degeneracy. As Edelman and Gally (2001) pointed out:

"Degeneracy is a prerequisite of natural selection because natural selection can only operate among a population of genetically dissimilar organisms." (p. 13766).

However, what are the limits of degeneracy? What factors influence degenerate systems, or more specifically, what tasks must these systems perform? To answer these questions, we need to consider evolutionary objectives and environmental demands.

A basic framework for understanding functional trade-offs in cognition, including natural and artificial cognitive systems, was proposed by Del Giudice and Crespi (2018).

The authors identified core functional properties shared by all systems, namely performance, efficiency, robustness, and flexibility (Figure 2.4). Among these properties, many functional trade-offs are possible.

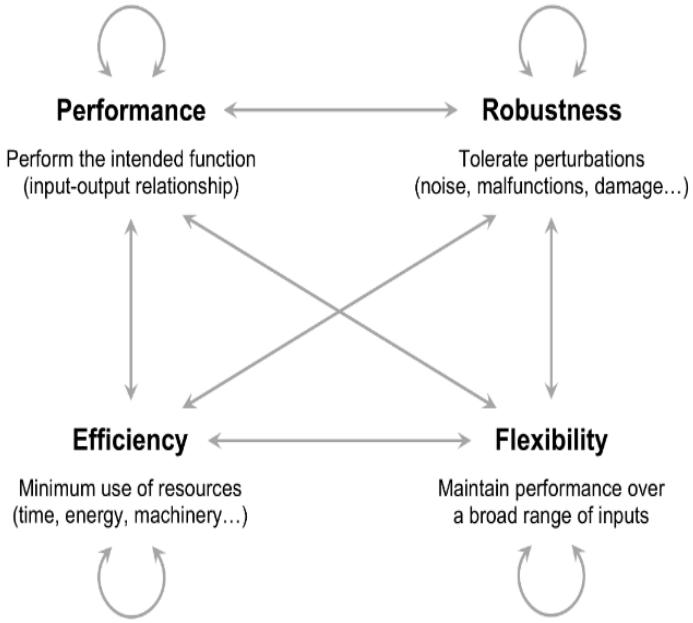

Figure 2.4: Trade-offs in cognitive systems. Basic functional properties and the tradeoffs among them. Also, trade-offs between the same property are possible because different aspects can be considered. Reproduced from Del Giudice and Crespi (2018).

In this thesis, we mainly focus on measuring the performance and efficiency of a system, specifically in CA1 pyramidal neurons in the rat hippocampus. Del Guidici and Crespi (2018) describe the two functions as follows:

"The performance of a system is usually defined as its ability to produce an intended result (or some other roughly equivalent formulation)" (Del Guidici & Crespi, 2018, p. 57), whereas

"The efficiency of a system is its ability to perform its function with minimal use of resources." (Del Guidici & Crespi, 2018, p. 58).

Enhancement is not free. Importantly, improving a system in one area often worsens it in others. This introduces the idea of Pareto optimality, which will be discussed in the next sub-chapter. However, it is important to understand that the 'design' of a

system does not require a conscious designer; notably, Darwinian biology shows that design and function can arise from the blind, undirected, and impersonal process of natural selection (Del Giudice & Crespi, 2018).

Computation can be quite energy-demanding, and the effort to reduce energy use seems to have shaped the evolution of neural systems, from the biophysical properties of neurons to brain connectivity (Del Giudice & Crespi, 2018). Pioneering work by Simon Laughlin and David Attwell (2001, 2015) clarified the roles of different processes in neural signaling within an 'energy budget' of the cell. They argued that over 80% of the energy in the brain's grey matter is used to generate action potentials and to support postsynaptic glutamatergic excitation. The remaining energy primarily supports the maintenance of the resting membrane potential and the recycling of glutamate (Attwell & Laughlin, 2001). They studied current flow at synapses in the visual pathway of the rat hippocampus and found that these synapses are optimized to maximize the information-to-energy ratio (Harris et al., 2015). Essentially, larger currents—which transmit information more accurately—can be achieved by increasing ion influx through postsynaptic channels; however, this increases the energy required to pump ions out and repolarize the membrane.

Laughlin also showed that neural transmission performance—measured by an improved signal-to-noise ratio—can be boosted by increasing the number of redundant synapses and/or their size, thereby raising energetic costs and requiring more cellular machinery. Consequently, larger synapses are typically found in neurons that perform high-precision computations (Laughlin, 2001; Sterling & Laughlin, 2015). Similarly, axons with larger diameters and/or thicker myelin sheaths can transmit information faster and with better signal-to-noise ratios. At the same time, they require greater amounts of lipids and proteins to build and occupy more space, leading to increased white matter volume and higher energy demands for construction and maintenance (Wang et al., 2008).

2.3 Pareto Optimality

In balancing different evolutionary goals, one might assume that natural systems are designed to follow an optimality principle. This is where the idea of Pareto optimality becomes helpful. The concept of Pareto optimality was introduced by the Italian economist Vilfredo Pareto, who used it to analyze economic efficiency (Pareto, 2014). A

state is considered Pareto optimal if it represents the best possible compromise ("trade-off") among various criteria, meaning that improving one criterion would worsen another criterion. The Pareto front includes all Pareto-optimal configurations. When examining ion-channel degeneracy, we can ask questions such as what constraints exist on it, whether there is a guiding principle, and whether there are functional trade-offs.

Uri Alon and colleagues discussed Pareto optimality and its connection to biological systems in their 2012 Science paper. They point out that biological systems cannot be perfect for every evolutionary task. Instead, they propose that Pareto fronts can help identify the best trade-offs for specific phenotypes. Their research shows that optimal trade-offs are weighted averages between different archetypes—phenotypes specialized for single tasks, such as energy efficiency or performance (Shovel et al., 2012). They also explore the shape of Pareto fronts, which depends on the number of tasks being optimized. For two tasks, the Pareto front appears as a line, for three, as a triangle, and so on in the phenotypic or functional space. Examples include variations in molar size ratios in rodents leading to herbivore, faunivore, and omnivore phenotypes, differences in Darwin's finch beak shapes and body sizes, and gene expression in E. coli. Therefore, maximizing fitness becomes a multi-objective optimization problem that can be analyzed using the Pareto front concept (Shovel et al., 2012; Figure 2.5).

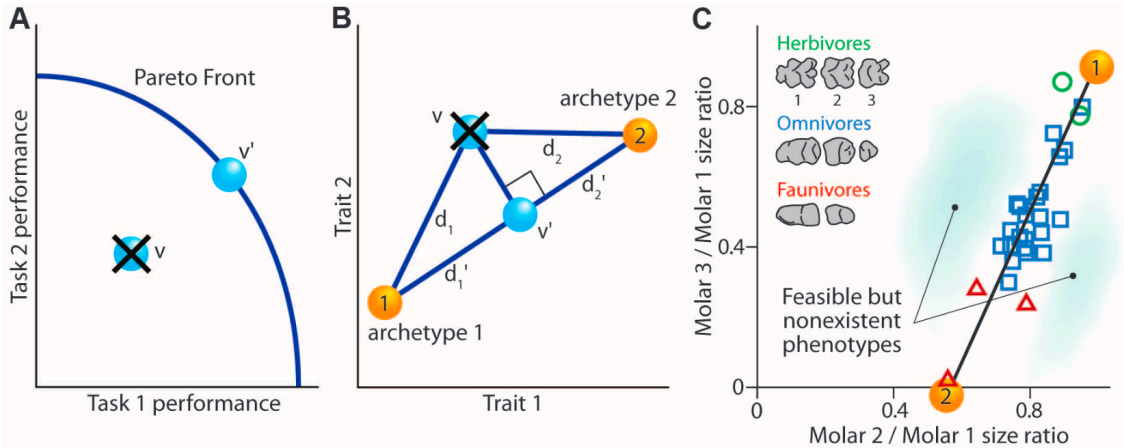

Figure 2.5: Overview of Pareto front. (A) The Pareto front (best trade-offs) shows what remains after removing (crossed-out symbol) all feasible phenotypes v that are dominated on all tasks by other feasible phenotypes v'. (B) The two archetypes in morphospace maximize performance in tasks 1 and 2. Phenotype v is farther from both archetypes than v′, the projection of v onto the line segment connecting the archetypes. Therefore, v performs worse than v′ in both tasks, resulting in lower fitness. Removing all such points v, we are left with the Pareto front: the line segment connecting the two archetypes [unlike (A), axes are traits,

not performances]. (C) The area ratios of rodent molar regions show a linear relationship. Most of the morphospace is empty. Herbivores (circles), faunivores (triangles), and omnivores (squares) are indicated. Reproduced from Shovel et al. (2012).

Jedlicka et al. (2022) addressed some questions about ion channel degeneracy and Pareto optimality in their review on Pareto optimality in single neurons. The authors state that Pareto optimality provides a useful framework for balancing evolutionary trade-offs across multiple tasks. They suggest that Pareto optimality could serve as a guiding principle for addressing ion channel degeneracy by identifying subpopulations of conductance-based models that optimize the balance between efficiency and functionality (Jedlicka et al., 2022). Additionally, the Pareto front reveals valuable insights into model configurations. The high-dimensional parameter space of neuronal models can be reduced to lower-dimensional manifolds, which may explain experimentally observed ion channel correlations (Jedlicka et al., 2022; Figure 2.6).

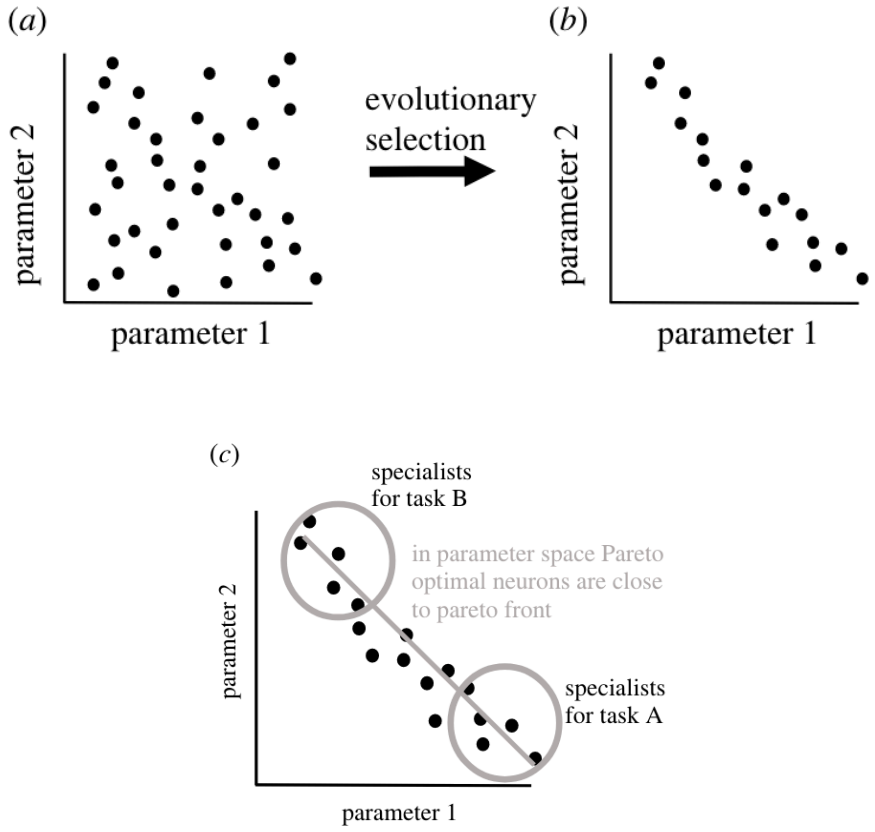

Figure 2.6: Pareto optimality can limit the parameter space for multiple tasks (functions), reducing suboptimal points based on trade-offs. (a) The original ion channel parameter space includes all possible combinations of ion conductance values. (b) Real neurons narrow this space to a small subspace, eliminating inefficient or ineffective configurations for their specific tasks, such as energy efficiency,

dendritic computation, and robustness. (c) The constrained space was shaped by two tasks, resulting in a line or curve that mediates between two extremes (specialists). Neurons located in the middle of this line are considered generalists, as they perform adequately in both tasks A and B, but at the expense of being less optimal in the other. Reproduced from Jedlicka et al. (2022).

2.4 CA1 Place Cells

John O'Keefe and Jonothan Dostrovsky were the first to discover place cells in the 1970s (1971). A few years later, John O'Keefe and Lynn Nadel proposed a seminal, coherent theory in their book 'The Hippocampus as a Cognitive Map' (1978). Since then, additional discoveries, such as grid cells by the Mosers (2008) and head direction cells (Ranck, 1984), have supported the role of the hippocampus in spatial cognition. The hippocampus is one of the most studied regions in the brain, making it an ideal system for neuroscientists to examine.

Spatial cognition is closely connected to the development of the hippocampus, especially its dorsal regions, including the entorhinal cortex, presubiculum, and parasubiculum, where cells exhibit place-dependent activity regardless of the animal's behavior or task (Moser et al., 2017). In this network of interconnected regions, input from the entorhinal cortex (EC) to the cornu ammonis 1 (CA1) subregion is essential for the formation of place fields. The hippocampal formation consists of three main structures: the dentate gyrus (DG), the hippocampus proper (Cornu Ammonis, CA), and the subiculum. The hippocampus proper is divided into CA1 (adjacent to the subiculum), CA2, and CA3 regions (Figure 2.7). The hilus serves as a boundary between the dentate gyrus and the CA3 region. The entorhinal cortex (EC) is a structure adjacent to the hippocampus that serves as a gateway for information flow to and from the hippocampal formation (Amaral & Witter, 1989).

"Key among these insights were the discoveries of place cells, head direction cells, and grid cells, each of which represent quantum jumps in our understanding that there is a system in the brain that has evolved to produce a representation manifold that can be linked to position (grid cells), an inertial compass (head direction cells), and a system for mapping external features and events onto internal and, at least locally, metric coordinates (place cells)." (Moser et al., 2017, p. 1448).

After recording from freely moving rats, O'Keefe and Dostrovsky observed that a small group of CA1 neurons showed activity that was location-dependent. This led them to propose that the hippocampus may create a spatial map (Moser et al., 2017; Figure 2.8). Specifically, they suggested that spatially localized firing mainly results from the dynamic integration of self-motion cues (Moser et al., 2017). O'Keefe early on recognized that these representations could depend on the fact that information about the changes in position and direction in space could be calculated from the animal's movement (O'Keefe, 1976). Different neurons had distinct place fields, allowing the animal's location to be inferred from the combined activity of a relatively small number of neurons at any given point in space (Moser et al., 2017). Place fields aligned with external cues and rotated accordingly to stay consistent when the cues were moved between sessions (Moser et al., 2017). Place cells completely stopped firing when animals were restrained from moving. Additionally, variation in place field size along the hippocampal septotemporal axis was strongly associated with the gain of physiological speed signals (Moser et al., 2017). In conclusion, these early lines of experiments robustly established the notion of place cells in the hippocampus, especially with respect to CA1.

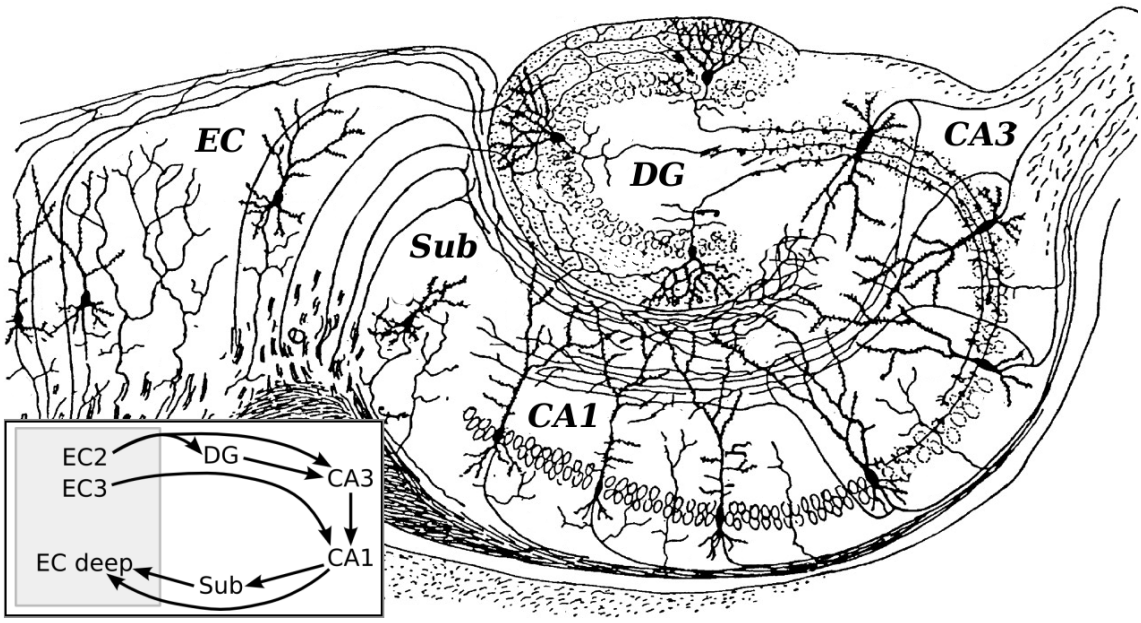

Figure 2.7: The hippocampal formation. Anatomy and main pathways in the hippocampus. EC = entorhinal cortex, DG = dentate gyrus, CA3 = CA3 region, CA1 = CA1 region, Sub = subiculum. Reproduced from Wikipedia, based on a drawing by Santiago Ramón y Cajal from his book "Histologie du système nerveux de l'homme & des vertébrés" (1911).

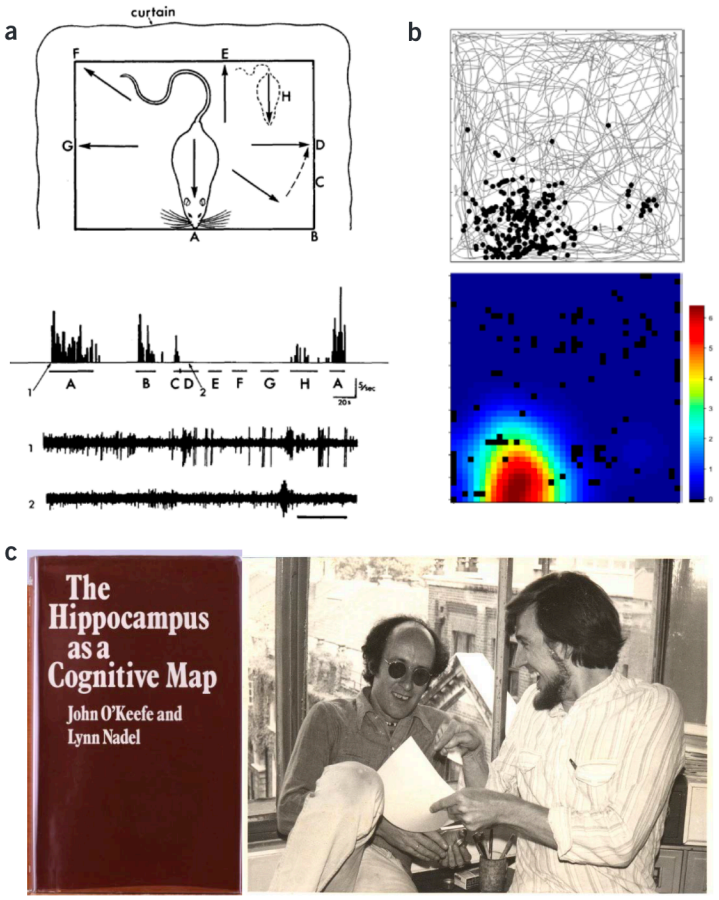

Figure 2.8: An Overview of the history of place cells. (a) Description of the first-place cell. Arrows and letters mark where the animal was restrained as it was pushed or coaxed around the test platform. The firing rate of the neuron is shown by the frequency histograms in the middle of the figure. Letters indicate positions, and lines show periods of restraint. The bottom lines display spikes at the start of the neuron response at A (1) and during the absence of a response at D (2). Calibration bar, 400 ms. Note that the cell responds selectively at only a few positions. O'Keefe and Dostrovsky reported that 8 of 76 recorded hippocampal cells responded only or mostly when the rat was in a specific part of the testing platform and facing a certain direction. (b) A place field as commonly shown today. Top: rat's trajectory in gray; spike locations superimposed as black dots—bottom: color-coded rate map; dark red indicating maximum rate; blue indicating silence. Areas not visited are in black. (c) Left: the book by John O'Keefe and Lynn Nadel was long a 'bible' in the study of spatial coding in the hippocampal formation. Right: Nadel (left) and O'Keefe (right) preparing the book. Reproduced from Moser et al. (2017).

3 Methods

We describe the methods used in this thesis, starting with the computational software NEURON, which is central to this work (3.1). Next, we explain the classification of the base model, including an overview of passive model parameters (3.2), active

conductances (3.3), synaptic input (3.4), place-field simulation (3.5), and output measures (3.6). Following this, we outline the information-theoretic analysis (3.7), our energy-theoretic analysis (3.8), the calculation of the Pareto front (3.9), our stochastic-search procedure (3.10), and additional computational details (3.11).

3.1 NEURON

Theoretical neuroscience is an emerging field that has been gaining importance since the mid-20th century. The pioneering work of Nobel laureates Alan Hodgkin and Andrew Huxley on the generation and propagation of action potentials in the squid giant axon (1952a, 1952b, 1952c) established the foundation for the field. Biologically realistic modeling is essential for testing hypotheses about the mechanisms believed to control neural signals and how the nervous system's function emerges from the operation of these mechanisms.

One of the most popular software packages in the field is the NEURON simulation environment developed at Stanford by Michael Hines and Nicholas Carnevale (1997, 2006). The software offers a tool for cross-validating data, estimating parameters that are difficult to measure experimentally, and determining whether known facts can account for experimental observations. It also serves to test hypotheses and identify the minimal set of anatomical and biophysical properties required to explain specific phenomena. The NEURON simulation platform provides a powerful and versatile environment for creating models of individual neurons and small neuronal networks (Hines & Carnevale, 1997).

Specifically, NEURON is based on the Hodgkin-Huxley axioms and Wilfried Rall's (1989) cable theory. It offers a framework for solving problems in which membrane properties vary spatially and membrane currents are complex (Hines & Carnevale, 1997). The branched structure typical of most neurons is incorporated by combining these equations with suitable boundary conditions (Hines & Carnevale, 1997). NEURON is especially useful for exploring new types of membrane channels because they are described using a high-level neuron model description language (NMODL) (Moore & Hines, 1996), which allows models to be represented as kinetic schemes or as sets of simultaneous differential and algebraic equations. NEURON also provides tools that handle the complex geometry and nonlinearities of biologically realistic models without

sacrificing its ability to work with more abstract and theoretical models (Hines & Carnevale, 1997).

3.2 The Base Model

This model is based on the paper by Roy and Rishikesh (2021). We briefly outline the key points relevant to our work. For a detailed overview, readers can refer to the original paper.

We used a morphologically accurate reconstruction of a rat hippocampal CA1 pyramidal neuron (Neuromorpho.org, cell ID n123; Ascoli, Donohue, & Halavi, 2007; Figure 3.1A). Passive membrane properties included axial resistivity (Ra), specific membrane capacitance (Cm), and distance-dependent membrane resistivity (Rm). The neuron was divided based on the dλ rule (Carnevale & Hines, 2006), so that each compartment was less than one-tenth of the electrotonic length constant at 100 Hz. This led to 879 compartments.

The non-uniform membrane resistivity followed a sigmoidal profile along the somato-dendritic axis (Basak & Narayanan, 2018; Golding et al., 2005; Narayanan & Johnston, 2007; Rathour & Narayanan, 2014):

$$R_m(x) = R_m^{soma} + \frac{R_m^{end} - R_m^{soma}}{1 + \exp\left(\frac{R_m^{hmp} - x}{R_m^{slope}}\right)} \quad (1)$$

where x is the radial distance from the soma, and the parameters define the maximum (R_m^{soma}), minimum (R_m^{end}), half-maximal point (R_m^{hmp}), and slope (R_m^{slope}) of the sigmoid.

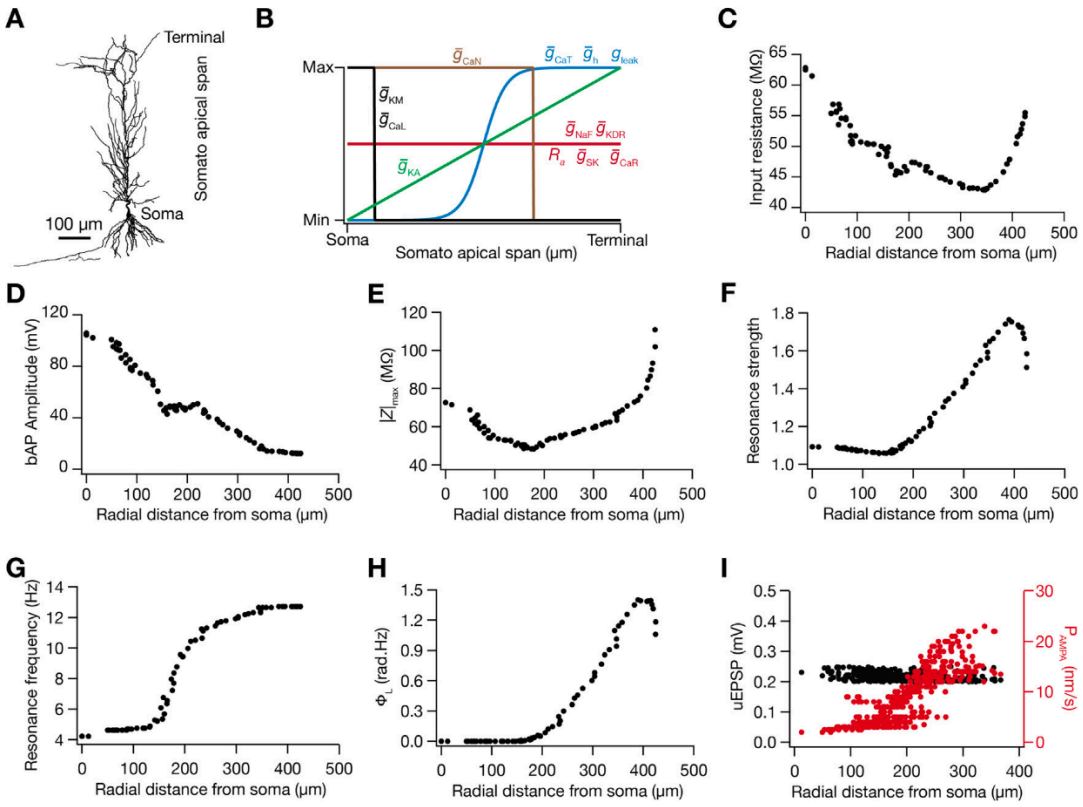

Figure 3.1: Base model of rat hippocampal CA1 pyramidal neurons, showing their intrinsic and synaptic properties along the somato-apical trunk. (A) Two-dimensional reconstruction of the 3D morphologically realistic model employed in this study. (B) Distribution of parameters governing the passive properties (gleak and Ra) and ten different active ion channels (gh, gNa, gKDR, gKA, gKM, gSK, gCaN, gCaL, gCaR and gCaT) along the somato-apical span to match multiple intrinsic measurements at the soma and along the apical dendrites, including input resistance (C), backpropagating action potential amplitude (D) maximum impedance amplitude (E), strength of resonance (F) resonance frequency (G), total inductive phase (H) and the maximum AMPAR permeability (I), all as functions of radial distance from the soma. The distance-dependent profile of maximum AMPAR permeability, PAMPA (I, right vertical axis), was set such that the somatic unitary excitatory postsynaptic potentials (uEPSPs) were around 0.2 mV, irrespective of synaptic location (I, left vertical axis). Reproduced from Roy and Narayanan (2021).

3.3 Active Conductances

The base model includes ten experimentally validated ion channel types: fast sodium (NaF), delayed rectifier potassium (KDR), A-type potassium (KA), M-type potassium (KM), small-conductance calcium-activated potassium (SK), T-type calcium (CaT), N-type calcium (CaN), R-type calcium (CaR), L-type calcium (CaL), and hyperpolarization-activated cyclic nucleotide-gated channels (HCN).

Sodium and potassium currents were modeled using Ohmic formulations with reversal potentials of +55 mV and –90 mV, respectively, and extracellular [Na+] and [K+] of 50 nM and 2 mM, respectively.

Spatial gradients were applied to several channels:

- KA conductance increased linearly with distance (Hoffman et al., 1997; Figure 3.1B):

$$g_{KA}(x) = g_{KA}^{soma}\left((1 + \frac{g_{KA}^{fold}}{100}x\right) \quad (2)$$

- HCN and CaT conductances followed sigmoidal increases with distance (Magee, 1998; Narayanan & Johnston, 2007; Figure 3.1B):

$$g_h(x) = g_h^{soma}\left((1 + \frac{g_h^{fold}}{1 + \exp\left(\frac{g_h^{hmp} - x}{g_h^{slope}}\right)}\right) \quad (3)$$

$$g_{CaT}(x) = g_{CaT}^{soma}\left((1 + \frac{g_{CaT}^{fold}}{1+\exp\left(\frac{g_{CaT}^{hmp} - x}{g_{CaT}^{slope}}\right)}\right) \quad (4)$$

Other channels were localized perisomatically (KM, CaL; Hu, Vervaeke, & Storm, 2007; Magee & Johnston, 1995; Figure 3.1B) or uniformly distributed (NaF, KDR, SK, CaR, CaN; Migliore et al., 1995; Poirazi, Brannon, & Mel, 2003; Figure 3.1B).

3.4 Synaptic Input

The model received 80 excitatory synapses randomly distributed across the apical dendritic tree. Each synapse contained colocalized AMPA and NMDA receptors with a fixed permeability ratio (PNMDA: PAMPA = 1.5). Permeabilities were adjusted so that all synapses generated somatic EPSPs of approximately 0.2 mV, regardless of their dendritic location (Andrasfalvy & Magee, 2001; Magee & Cook, 2000; Figure 3.1I).

NMDA currents were computed as the sum of Na^+, K^+, and Ca^{2+} fluxes, modeled using the GHK equation with Mg^{2+} block (Jahr & Stevens, 1990):

$$I_{NMDA}(v,t) = I_{Na}(v,t) + I_K(v,t) + I_{Ca}(v,t) \quad (5)$$

$$MgB(v) = \left(1 + \frac{[Mg]_o}{3.57}\exp\left(-0.062v\right)\right)^{-1} \quad (6)$$

AMPA currents followed Ohmic formulations for Na^+ and K^+, with kinetics defined by exponential rise and decay (τ_r= 2 ms, τ_d= 10 ms).

$$I_{AMPA}(v,t) = I_{AMPA}^{Na}(v,t) + I_{AMPA}^{K}(v,t) \quad (7)$$

3.5 Place-Field Simulation

One important computational feature of our model is the presynaptic input, which should mimic place-cell inputs to the neuron. Their firing rates are modeled stochastically, driven by a Gaussian-modulated cosine function (Roy & Narayanan, 2021). The presynaptic firing triggers the opening of colocalized synaptic NMDAR and AMPARs, resulting in synaptic currents flowing into the model neuron (Roy & Narayanan, 2021). The Gaussian-modulated cosinusoidal function that governs the probability of a presynaptic spike occurring at each synapse in the neuron was calculated as:

$$F_{pre}(t) = F_{pre}^{max}\left(1 + cos\left(2\pi f_0 (t - T)\right)\right)\exp\left(-\frac{(t - T)^2}{2\sigma^2}\right) \quad (8)$$

Where F_{pre}^{max} is the maximal input firing-rate. Presynaptic activity was modeled as a Gaussian-modulated cosine wave, corresponding to an 8 Hz theta rhythm (Basak & Narayanan, 2018; Seenivasan & Narayanan, 2020) with center T = 5, frequency f_0 = 8 Hz, and Gaussian width σ = 1 s.

3.6 Output Measures

Spikes were detected by thresholding the somatic membrane potential to -20 mV. Firing rates were estimated by convolution of spike trains with a Gaussian kernel (σ = 200 ms). Place-field sharpness was assessed via maximum firing rate (F_{max}) and full-width at half-maximum (FWHM). Subthreshold ramps were extracted by median filtering (0.75 s window). Theta modulation was quantified from the Fourier spectrum of filtered traces (50 ms window) (Harvey et al., 2009).

To validate intrinsic properties of the modeled neuron, we performed standard electrophysiological measurements at different somatodendritic locations.

- Input resistance (R_{in} ; Figure 3.1C): computed by injecting a –100 pA hyperpolarizing current pulse of 500 ms duration into the target compartment and measuring the steady-state voltage deflection. Rin was defined as the ratio of voltage deflection to current amplitude (Basak & Narayanan, 2018).

- Back-propagating action potential (bAP; Figure 3.1D): triggered by a 1 nA, 2 ms current injection at the soma. The amplitude of the resulting action potential was measured at the soma and at various apical trunk locations to assess active back-propagation.

- Impedance-based measurements (Figure 3.1E-H): To assess frequency-dependent response properties (Basak & Narayanan, 2018, 2020; Narayanan & Johnston, 2007, 2008; Narayanan, Dougherty, & Johnston, 2010; Rathour & Narayanan, 2014), a chirp current stimulus (peak-to-peak amplitude 100 pA; frequency sweep 0–15 Hz over 15 seconds) was injected into the compartment of interest. Voltage responses were Fourier transformed and divided by the input current spectrum to obtain the complex impedance profile.

  The magnitude of impedance was defined as:

$$|Z(f)| = \sqrt{(Re(Z(f)))^2 + (Im(Z(f)))^2} \quad (9)$$

The resonance frequency (f_R) was identified as the frequency of maximum $|Z(f)|$. Resonance strength (Q) was calculated as the ratio of the maximum impedance amplitude to the impedance at 0.5 Hz.

The phase profile was defined as:

$$\phi(f) = \tan^{-1}\frac{Im(Z(f))}{Re(Z(f))} \tag{10}$$

The total inductive phase (ϕ_L) was quantified as the area under the positive portion of the phase profile.

3.7 Information-Theoretic Analysis

To obtain location-independent spatial information transfer, we computed the mutual information between firing-rate responses (F) and spatial location (S) across the entire place field (Butts, 2003; Butts & Goldman, 2006; DeWeese & Meister, 1999; Roy & Narayanan, 2021). For this analysis, the place field was discretized into 20 spatial bins, each further subdivided into 4 sub-bins, yielding 80 spatial states. The instantaneous firing-rate response was quantized into 20 bins. Mutual information (MI) was then calculated as the information transfer between the spatial stimulus (S) and firing-rate response (F), aggregated across all locations. The mutual information was defined as:

$$I\,(F\,;\,S)\;=\;H\,(F)\;-\;H\,(F\,|S) \tag{11}$$

where:

$$H(F) = -\sum_j p(F_j)\log_2 p(F_j) \tag{12}$$

is the entropy of firing rates across all spatial positions, and:

$$H(F|S) = -\sum_k p(S_k)\sum_j p(F_j|S_k)\log_2 p\left(F_j\middle|S_k\right) \tag{13}$$

is the conditional entropy of firing rates given spatial bins S_k.

Here, $p(F_j)$ denotes the probability of observing firing rate bin j across the entire trajectory, while $p(F_j|S_k)$ is the probability of observing firing rate bin j given that the animal is in spatial bin S_k. The spatial occupancy probability $p(S_k)$ was assumed to be uniform across bins.

Note that the number of spatial bins (80) and firing-rate bins (20) were not required to match. In information-theoretic analyses, the mutual information is computed from the joint probability distribution $p(S,F)$, which is well-defined regardless of the cardinalities of the stimulus set (S) and the response set (F) (Butts, 2003; DeWeese & Meister, 1999). Using more spatial bins than firing-rate bins, as in Roy & Narayanan (2021), provides sufficient resolution of the spatial variable while maintaining robust estimation of firing-rate distributions.

3.8 Stochastic-Search Procedure

A single hand-tuned model cannot capture the diverse biophysical differences across neuronal structures. Additionally, results from such a model might be biased by the specific parameter choices. A common method to address this issue is to create a population of models that collectively captures the variability observed in the neuronal subtype being studied (Goaillard et al., 2009; Goaillard & Marder, 2021; Jedlicka et al., 2022).

To achieve this, we used a multi-parameter and multi-objective stochastic search (MPMOSS) algorithm (Basak & Narayanan, 2018, 2020; Narayanan & Johnston, 2012). In this approach, multiple conductance and passive parameters were allowed to vary independently within ranges constrained by experimental data (Table 3.1). A large number of candidate models was generated via uniform random sampling over these ranges, ensuring an unbiased exploration of the parameter space. Each candidate was then tested against several electrophysiological benchmarks (Table 3.2).

Validation criteria included:

- Place-cell firing properties: sharpness of place-field tuning, quantified by maximum firing rate (F_{max}> 20 Hz) and full width at half maximum ($FWHM$< 2.5 s).

- Six canonical intrinsic functional maps (Basak & Narayanan, 2018, 2020; Narayanan & Johnston, 2012): back-propagating action potential amplitude (bAP), input resistance (R_{in}), resonance frequency (f_R), maximum impedance amplitude ($|Z|_{max}$), strength of resonance (Q), and total inductive phase (ϕ_L). Each of these six measurements was validated at three locations along the somato-apical trunk (soma, ~150 μm, and ~300 μm from soma), yielding 18 measurements.

- Firing responses to somatic current injections: firing rates in response to 100, 150, 200, and 250 pA step currents (4 measurements).

A total of 24 independent measurements (2 + 18 + 4) were used to identify valid models. Only models that met all physiological bounds were included in the final population.

To investigate parameter interdepencies, we calculated pairwise Pearson correlation coefficients across all valid models.

	Parameter (unit)	Symbol	Base value	Range
Passive properties				
R_a (uniform across the neuron)				
1	Axial resistivity (Ω-cm)	R_a	120	100–250
R_m (sigmoidal reduction with distance from soma)				
2	Maximum value (kΩ cm^{-2})	R_m^{soma}	125	62.5–250
3	Minimum value (kΩ cm^{-2})	R_m^{end}	85	42.5–170
4	Half-maximal point of sigmoid (μm)	R_m^{hmp}	300	150–600
5	Slope of sigmoid (μm)	R_m^{slope}	50	25–100
Active properties				
Spike-generating channels (uniform across all somatodendritic compartments)				
6	Maximum conductance for NaF (mS cm^{-2})	$\bar{g}_{Na}$	16	8–32
7	Maximum conductance for KDR (mS cm^{-2})	$\bar{g}_{KDR}$	10	5–20
HCN channel (sigmoidal increase with distance from soma)				
8	Maximum somatic conductance (μS cm^{-2})	$\bar{g}_h^{soma}$	25	12.5–50
9	Fold increase	$\bar{g}_h^{fold}$	12	6–24
10	Half-maximal point of sigmoid (μm)	$\bar{g}_h^{hmp}$	320	160–640
11	Slope of sigmoid (μm)	$\bar{g}_h^{slope}$	50	25–100
T-type calcium channel (sigmoidal increase with distance from soma)				
12	Maximum somatic conductance (μS cm^{-2})	$\bar{g}_{CaT}^{soma}$	80	40–160
13	Fold increase	$\bar{g}_{CaT}^{fold}$	30	15–60
14	Half-maximal point of sigmoid (μm)	$\bar{g}_{CaT}^{hmp}$	350	175–700
15	Slope of sigmoid (μm)	$\bar{g}_{CaT}^{slope}$	50	25–100
A-type potassium channel (linear increase with distance from soma)				
16	Maximum somatic conductance (mS cm^{-2})	$\bar{g}_{KA}^{soma}$	3.1	1.55–6.2
17	Fold increase per 100 μm	$\bar{g}_{KA}^{fold}$	8	4–16
N-type calcium channel (till 340 μm from soma in apical dendrites)				
18	Maximum conductance	$\bar{g}_{CaN}$	15	7.5–30
R-type calcium channel (dendritic localization)				
19	Maximum conductance in dendrites (μS cm^{-2})	$\bar{g}_{CaR}$	15	7.5–30
L-type calcium channel (perisomatic, till 50 μm from soma in apical dendrites)				
20	Maximum conductance (mS cm^{-2})	$\bar{g}_{CaL}$	1.20	0.6–2.4
Small-conductance calcium-activated potassium channel (dendritic localization)				
21	Maximum conductance of SK (μS cm^{-2})	$\bar{g}_{SK}$	1.5	0.75–3
M-type potassium channel (perisomatic, till 50 μm from soma)				
22	Maximum conductance (μS cm^{-2})	$\bar{g}_{KM}$	1	0.5–2

Table 3.1: Model parameters, their base values, and ranges for the stochastic-search procedure. For all parameters, the range uniformly spans from 0.5 to 2 times the respective base-model value. Reproduced from Roy and Narayanan (2021).

	Measurement	Soma		~150 μm		~300 μm	
		Lower	Upper	Lower	Upper	Lower	Upper
Intrinsic somatodendritic functional map measurements (18)							
1	Input Resistance (MΩ)	40	100	30	60	10	50
2	Maximum Impedance (MΩ)	50	110	35	80	20	80
3	Resonance frequency (Hz)	2	7	4	8	5	14
4	Strength of Resonance	1.01	1.5	1.01	1.9	1.2	2.6
5	Total Inductive Phase (rad Hz)	0	0.3	0	1	0.025	2
6	Backpropagating Action Potential (mV)	90	115	40	70	5	45
Action potential firing rate measurements (4)							
7	Firing rate for 100 pA current injection	0	20				
8	Firing rate for 150 pA current injection	0	30				
9	Firing rate for 200 pA current injection	0	40				
10	Firing rate for 250 pA current injection	5	45				
Measurements of place-cell tuning sharpness (2)							
11	Peak firing rate (Hz)	56	–				
12	Full Width at Half Maxima (s)	–	2.5				

Table 3.2 Intrinsic somatodendritic and functional measurements of CA1 place cells and their electrophysiological limits for model validation. Notice that the lower bound of the peak firing rate during place field traversal is 20 Hz in our population and not 56 Hz. Reproduced from Roy and Narayanan (2021).

3.9 Energy-Theoretic Analysis

Finally, we calculated the energy consumption as the total usage of adenosine triphosphate (ATP) during the place field traversal of the virtual animal in our simulations. The calculations are based on Remme et al. (2018) and Harris et al. (2015) and include ATP consumption for reversing sodium (Na) and calcium (Ca) influx during cell activity. In a biological neuron, this happens by virtue of the sodium-potassium pump, which transports three intracellular sodium ions out and two extracellular potassium ions in, against their respective concentration gradients, using one ATP molecule to phosphorylate the pump and change its conformation. Similarly, a calcium pump, such as the SERCA pump, uses one ATP molecule to pump two calcium ions out of the cell. To quantify the amount of sodium and calcium ions, we recorded the currents during our simulations (I_{Na} and I_{Ca}) . This can be converted to total ATP consumption by converting the integrated current (coulombs) to the number of elementary charges using the factor 6.242×10^{18} and dividing by 3 or 2, respectively (number of ions per ATP molecule). As these pumps are the main ATP consumers during cellular activity, sustaining the cell's

membrane potential homeostasis, the following ion-counting methods approximate the energy consumption required for the reversal of cellular activity:

$$ATP_{Na} = \frac{1}{3} \times I_{Na} \times 6.242 \times 10^{18} \quad (14)$$

for sodium. And:

$$ATP_{Ca} = \frac{1}{2} \times I_{Ca} \times 6.242 \times 10^{18} \quad (15)$$

for calcium, respectively.

3.10 Pareto Front Calculation

To derive the Pareto front of our model population, we filtered models for the two competing objectives of effectiveness and efficiency. Meaning we searched for models that simultaneously maximized MI and minimized ATP consumption. A model is Pareto optimal if no other model is better in both objectives simultaneously. If such a model exists, then the previous model (i) is dominated, because the new model (j) achieved better or equal MI while consuming equal or less ATP. Logically, this can be expressed as:

$$F(MI_i, ATP_i) \leq F\left(MI_j, ATP_j\right) \quad (16)$$

Where F is our fitness function that maximizes MI and minimizes ATP. Equivalent to:

$$F = \max(MI, -ATP) \quad (17)$$

3.11 Computational Details

All simulations were conducted using custom-written software in the NEURON simulation environment (Carnevale & Hines, 2006), at 34°C with an integration time step

of 25 µs. Unless otherwise noted, all simulations used a resting potential of −65 mV. Analysis was carried out using custom software written in Python and MATLAB 2024a.

4 Results

Results are organized around three complementary analyses. We first characterize the intrinsic and functional properties of model neurons that satisfied all experimentally informed criteria (4.1), then examine the parameter configurations of this population and the degree of degeneracy they exhibit (4.2), and finally quantify the trade-offs between energy (ATP) and information (MI) transmission that give rise to an emergent Pareto front (4.3). An overview of the experimental procedure is provided in Figure 4.1.

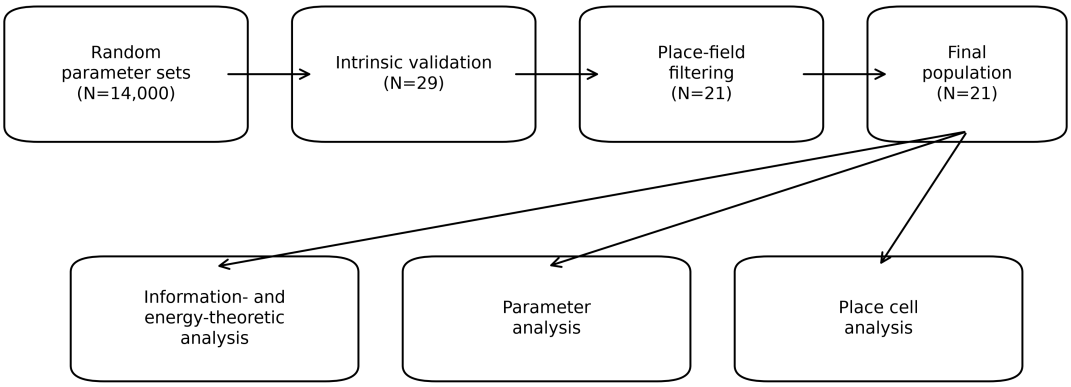

Figure 4.1 Overview of experimental procedure.

4.1 Place Cell Properties

After generating our initial model population (N=14,000), we run simulations using different experimental measurements to constrain the population. The intrinsic and functional properties included input resistance, maximum impedance, resonance frequency, resonance strength, inductive phase, and bAP amplitude – all measured at three distinct somatodendritic locations (soma, 150 µm, and 300 µm along the apical trunk). Moreover, we injected current into the somatic compartment in silico and measured the firing rate response at 100, 150, 200, and 250 pA. After this procedure, our

initial population shrank to N=29 validated models. Lastly, we simulated virtual place field traversal and validated place field properties, such as peak firing rate and FWHM. In total, 21 models passed all our intrinsic and functional experimental constraints (Figure 4.2A–I). Table 1 summarizes the mean values and standard deviations of the final population.

All the models were well within our imposed limits. Interestingly, measurements closer to the soma appear more tightly clustered, whereas farther along the apical trunk, they become more scattered (Figure 4 A-F). For example, the distribution of the inductive phase at the soma (mean = 0.02 rad x Hz, STD = 0.02 rad x HZ) and 150 micrometers (mean = 0.04 rad x Hz, STD = 0.04 rad x HZ) away along the somatodendritic trunk in comparison to 300 micrometers (mean = 0.65 rad x Hz, STD = 0.39 rad x HZ) away. In addition, the distribution of the bAP at the soma (mean = 107.7 mV, SD = 3.66 mV) and 150 μm (mean = 52.79 mV, SD = 4.02 mV) along the apical trunk in comparison to 300 μm (mean = 27.09 mV, SD = 9.68 mV) away.

Moreover, we observed the greatest dropouts in our population at the distal locations for resonance strength, inductive phase, and bAP. This means that either our experimental constraints were very strict and/or that only a small subset of ion channel configurations is rendered functional in these regimes. In particular, a positive inductive phase, in which the voltage response leads the current stimulus, is highly dependent on low-threshold-activated currents, such as HCN and A-type potassium currents. Lastly, our place field constraints might have prevented greater variance in place field properties. Overall, our model populations' place-cell characteristics satisfy intrinsic and functional neural metrics while remaining tightly constrained within functional space.

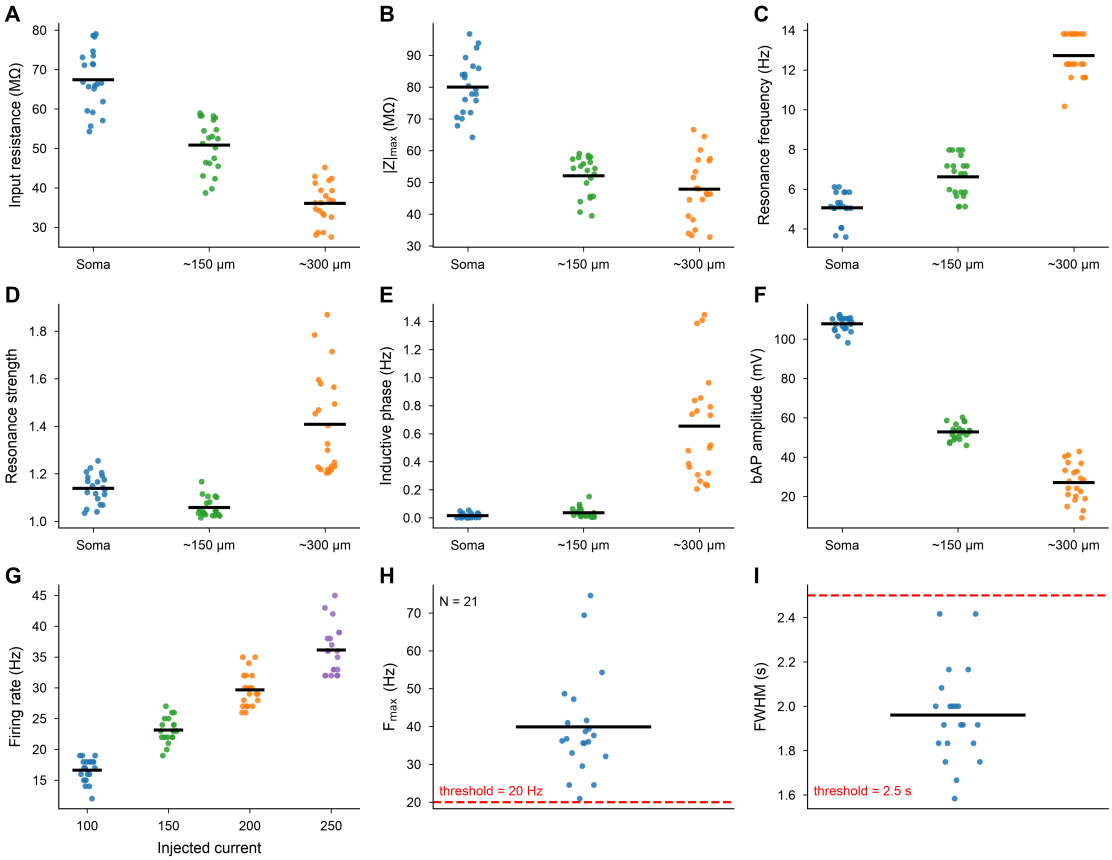

Figure 4.2 Population summary of intrinsic electrophysiological and functional properties across somatic and dendritic locations. Each point represents an individual model. Black horizontal bars indicate mean values. The population reproduces experimentally constrained ranges for input resistance (A), impedance amplitude (B), resonance frequency (C), resonance strength (D), inductive phase (E), and bAP amplitude (F). Firing rates across injected currents are shown in (G). Place-field peak firing rate (H) and width (I) satisfy selection thresholds (red dashed lines).

Measurement	Value
Input resistance (Soma)	67.41 ± 7.55 MΩ
Input resistance (~150 µm)	50.82 ± 6.49 MΩ
Input resistance (~300 µm)	36.08 ± 5.18 MΩ
$\|Z\|_{max}$ (Soma)	80.00 ± 8.92 MΩ
$\|Z\|_{max}$ (~150 µm)	52.08 ± 6.19 MΩ
$\|Z\|_{max}$ (~300 µm)	47.88 ± 10.16 MΩ
Resonance frequency (Soma)	5.06 ± 0.78 Hz
Resonance frequency (~150 µm)	6.62 ± 1.02 Hz
Resonance frequency (~300 µm)	12.72 ± 1.08 Hz
Resonance strength (Soma)	1.14 ± 0.06
Resonance strength (~150 µm)	1.06 ± 0.04
Resonance strength (~300 µm)	1.41 ± 0.21
Inductive Phase (Soma)	0.02 ± 0.02 rad Hz
Inductive Phase (~150 µm)	0.04 ± 0.04 rad Hz
Inductive Phase (~300 µm)	0.65 ± 0.39 rad Hz
bAP amplitude (Soma)	107.70 ± 3.66 mV
bAP amplitude (~150 µm)	52.79 ± 4.02 mV
bAP amplitude (~300 µm)	27.09 ± 9.68 mV
Firing rate (100 pA)	16.62 ± 1.91 Hz
Firing rate (150 pA)	23.14 ± 1.98 Hz
Firing rate (200 pA)	29.67 ± 2.78 Hz
Firing rate (250 pA)	36.14 ± 3.88 Hz
F_{max}	39.90 ± 13.33 Hz
FWHM	1.96 ± 0.21 s

Table 4.1 Summary of mean values and standard deviations for intrinsic and functional measurements of the final population.

4.2 Parameter Degeneracy

Next, we set out to determine the distribution of the parameters of our final model population. Therefore, we assessed parameter variability by calculating pairwise correlations among all our model parameters. We received scatter plots showing weak to moderate correlations among model parameters, confirming parameter degeneracy. Figure 4.3 shows a color-coded correlation matrix of pairwise correlation coefficients for an overview. These results indicate, notably, that different neural substrates can give rise to similar functional properties while remaining independent of ion-channel conductances

and passive kinetic properties. These results confirm decades of neuroscience research and add to the evidence for intrinsic degeneracy.

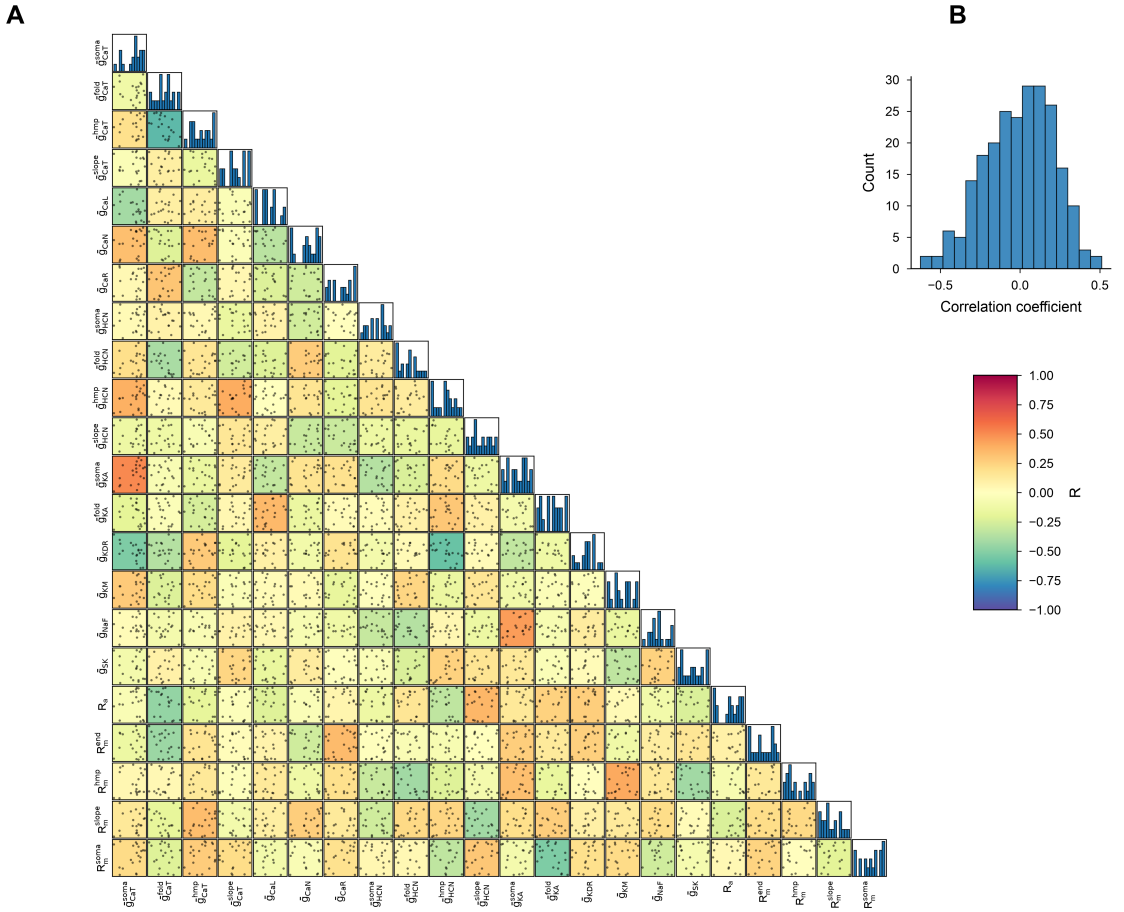

Figure 4.3 Pairwise correlation matrix of model parameters across the valid population. (A) Each panel shows the relationship between two parameters, with color indicating the correlation coefficient. The predominance of weak correlations indicates a high degree of independence between parameters, consistent with degeneracy. (B) Histogram of the correlation coefficients derived from the scatter plots in panel A.

Interestingly, the strongest positive correlation observed in our model population (r = 0.512) was between the A-type potassium conductance (gKA) and the T-type calcium conductance (gCaT; Figure 4.4). This likely indicates an antagonistic, tightly coupled relationship: gCaT excites the cell, promoting depolarization and spike initiation, while gKA counteracts this by delaying or suppressing firing. The interplay between these two channels ultimately yields a similar firing pattern, exemplifying a degenerate mechanism that produces comparable functional output from different ion channel configurations.

Additionally, the fast-gated sodium conductance (gNa) shows a high correlation (r = 0.452) with gKA, suggesting another form of homeostatic regulation operating

antagonistically (Figure 4.5). Moreover, significant negative correlations were observed between gCaT and delayed rectifier potassium conductance (gKDR; r = -0.531), the fold increase in gKA (gKAfold) and the somatic membrane resistance (rmsoma; r = -0.526), the half-maximal point of gh's sigmoidal distribution (ghhmp) and gKDR (r = -0.592), and the fold increase in gCaT (gCaTfold) and the half-maximal point of gCaT's sigmoidal distribution (gCaThmp; r = -0.626; Figures 4.6 – 4.9). Many of these patterns can be explained by biophysical principles. The balance between gKAfold and the rmsoma reflects a competition for neural excitability across compartments. According to Ohm's law (V = I x R), the somatic membrane resistance determines how much a given current depolarizes the soma to trigger spiking, while gKAfold acts to repolarize the membrane along the somatodendritic axis. When rmsoma decreases, the soma becomes leakier due to reduced isolation, so gKAfold must offset increased input along the axis, requiring a higher current to activate the neuron.

Another compensatory mechanism might operate between gCaT and gKDR. Since gCaT is a low-threshold inward current that excites the neuron, and gKDR helps repolarize it and suppress activity, a simple view would suggest a positive correlation if considering only the direct causal link within a neuron. However, in our degenerative population, other mechanisms might maintain this balance, such as gCaT versus gKA, as previously noted. Consequently, a negative correlation between gCaT and the gKDR could be observed if another mechanism already compensates for this interaction.

The hyperpolarization-activated cyclic nucleotide-gated (HCN) channel passes sodium and potassium ions in a 1:4 ratio, producing a net depolarizing current. Unlike most voltage-gated channels, HCN is already active at resting membrane potential and is further recruited by hyperpolarization (Mishra & Narayanan, 2023). This creates the conditions for negative feedback: hyperpolarization recruits HCN, producing a depolarizing current that opposes the perturbation, while depolarization reduces HCN activity, withdrawing that restoring drive. The channel thus enforces a homeostatic set point around which membrane voltage is continuously stabilized – a property that positions ghhmp as a key regulator of this feedback along the somatodendritic trunk.

Since gKDR also regulates neuronal activity by repolarizing neurons and suppressing neuronal activity, it is plausible that the expression of both channels is redundant. Therefore, increasing one channel's expression would likely cause a decrease in the other.

Finally, the negative correlations between gCaTfold and gCaThmp are related to each other. Both factors increase gCaT expression along the somatodendritic trunk. Since one mechanism should suffice, the other becomes less relevant. This aligns with the interpretation of co-regulation as agonistic, in the sense that the function of one parameter mimics that of another.

The correlation between the spike-generating channels, gNa and gKDR remains relatively weak (r = 0.120). This may reflect the strict constraints imposed on our model population on firing behavior and place-field shape. Overall, the distinct biophysical properties of ion channels and the precise control of their combinations enable the neuron to maintain reliable functional output despite perturbations.

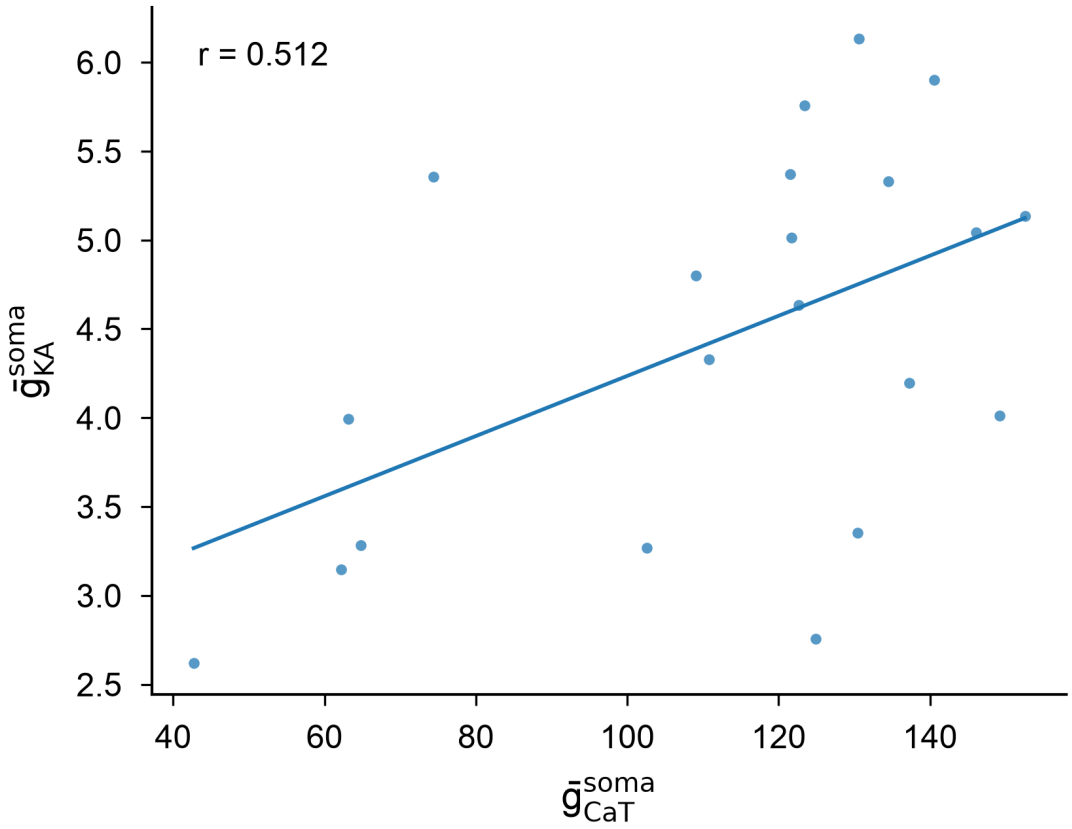

Figure 4.4 Pairwise correlation between A-type potassium conductance (gKA) and the T-type calcium conductance (gCaT) across the valid model population.

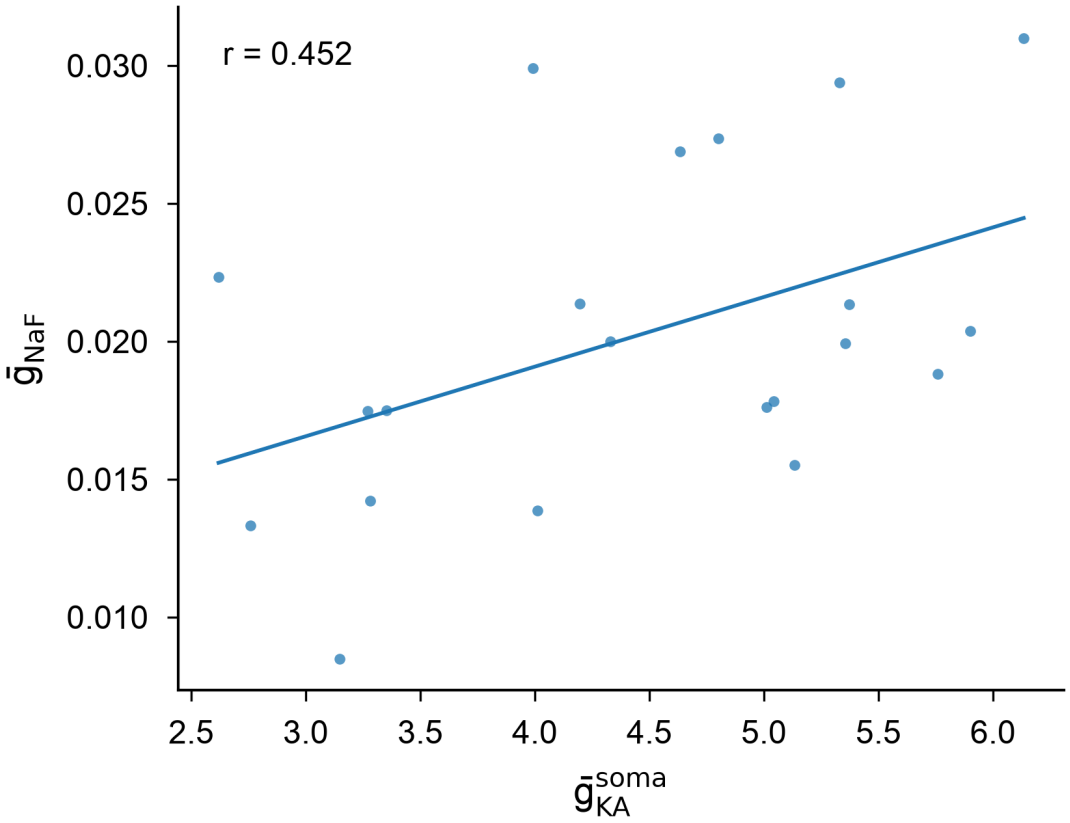

Figure 4.5 Pairwise correlation between fast-gated sodium conductance (gNa) and the A-type potassium conductance (gKA) across the valid model population.

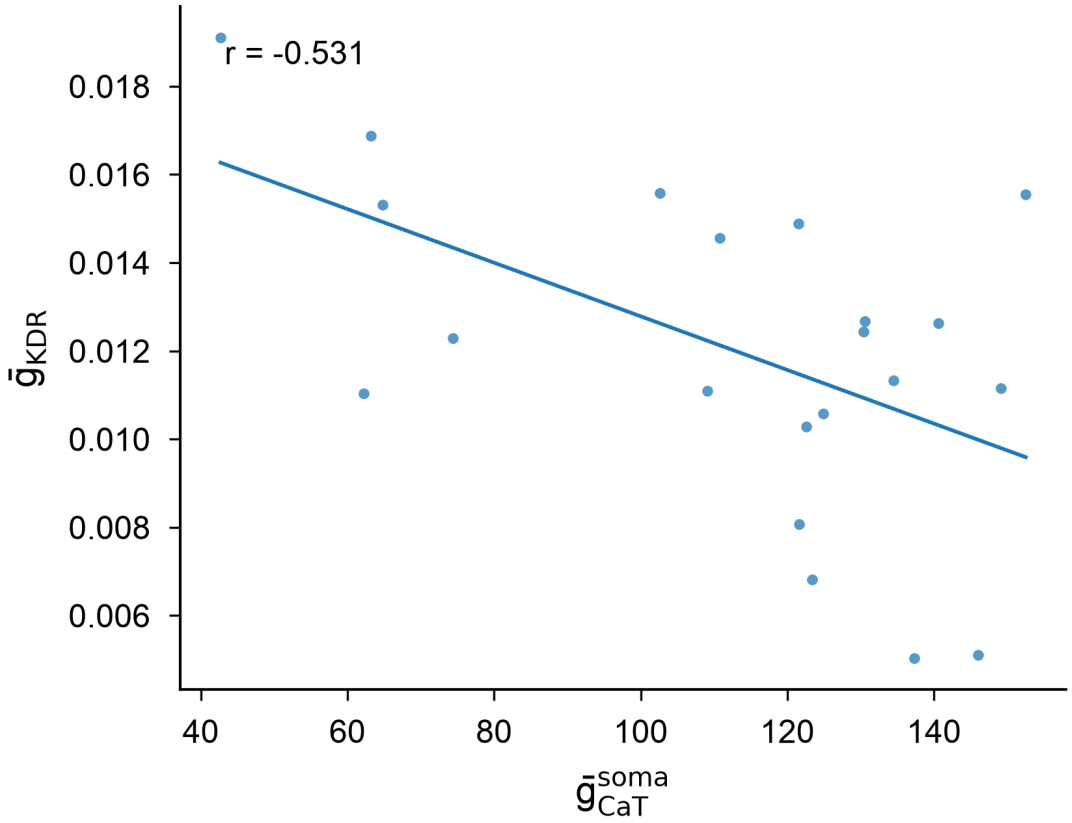

Figure 4.6 Pairwise correlation between the delayed rectifier potassium conductance (gKDR) and the T-type calcium conductance (gCaT) across the valid model population.

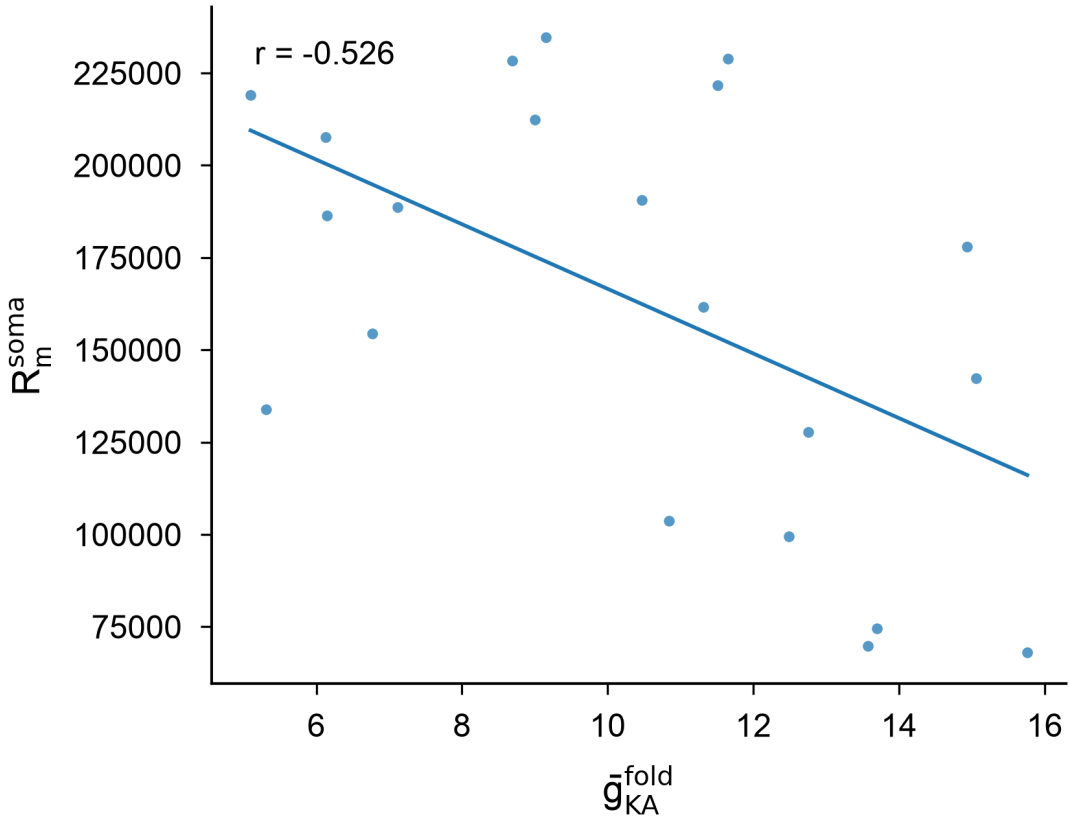

Figure 4.7 Pairwise correlation between the somatic membrane resistance (rmsoma) and the fold increase in the A-type potassium conductance (gKAfold) across the valid model population.

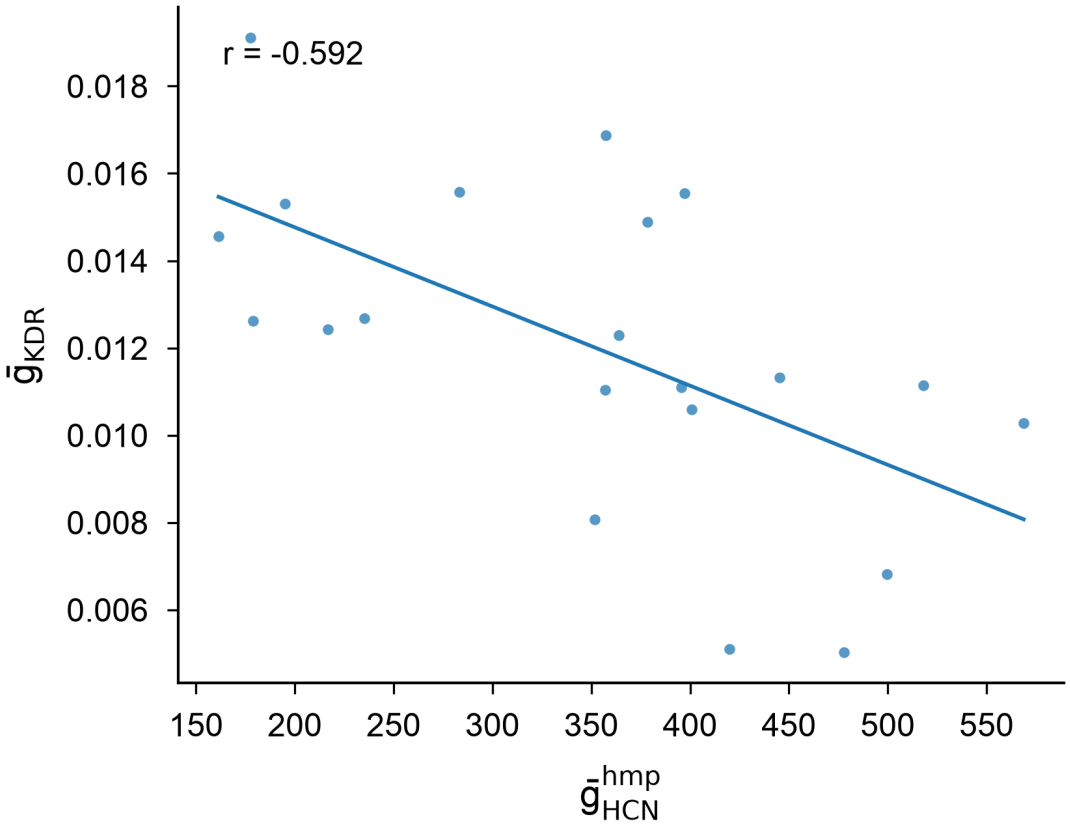

Figure 4.8 Pairwise correlation between the delayed rectifier potassium channel (gKDR) and the half-maximal point of the hyperpolarization-activated cyclic nucleotide-gated conductance's sigmoidal distribution (ghhmp) across the valid model population.

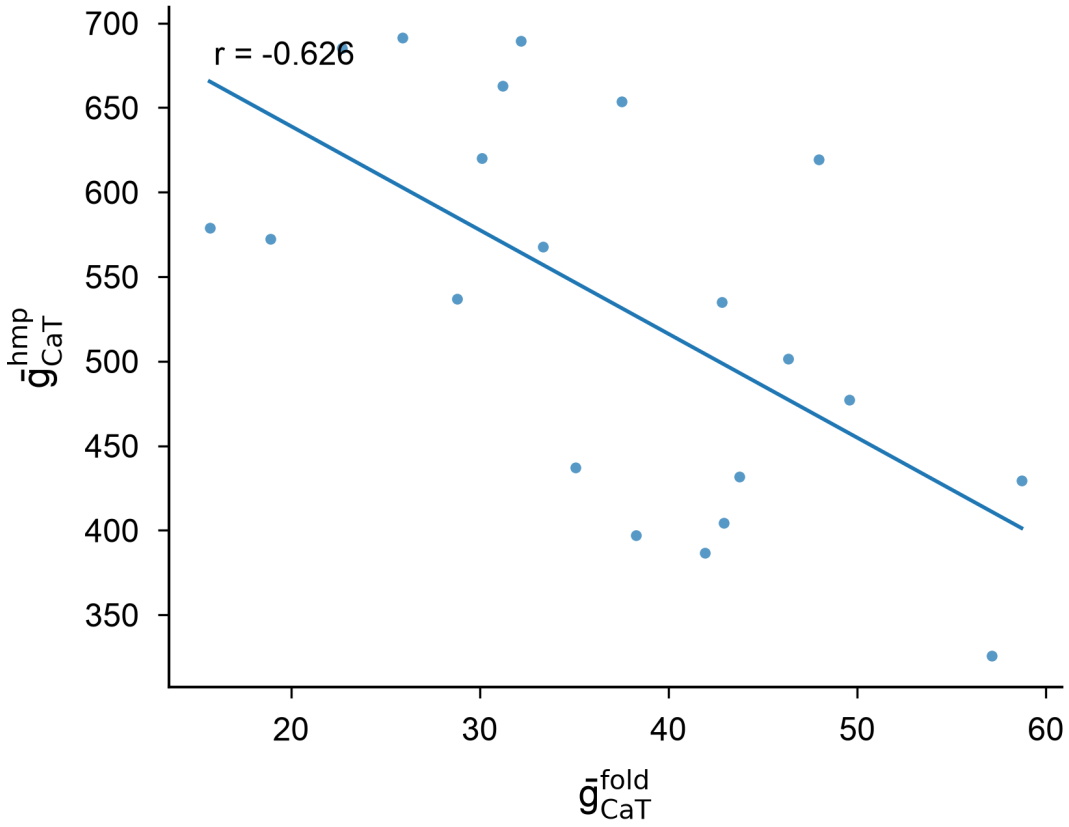

Figure 4.9 Pairwise correlation between the fold increase in the T-type calcium conductance (gCaTfold) and the half-maximal point of T-type calcium conductance's sigmoidal distribution (gCaThmp) across the valid model population.

Additionally, we recorded sodium, calcium, and synaptic currents – the main excitatory currents contributing to the formation of the place field – and measured their relative contribution during the place field traversal. Intriguingly, we observed variance in the underlying currents across models, while the place field shape and MI content remained essentially the same (Figures 4.10 – 4.12). This suggests that the recorded conductances can compensate for one another and confer robust, stable place coding on the models. Some conductances, such as gh and gCa, varied more than others, such as gAMPA and gNMDA, indicating that intrinsic conductances, rather than synaptic conductances, contribute to the variance in the model population. This exemplifies a hallmark of ion channel degeneracy: different ion channel configurations that yield similar input-output behavior.

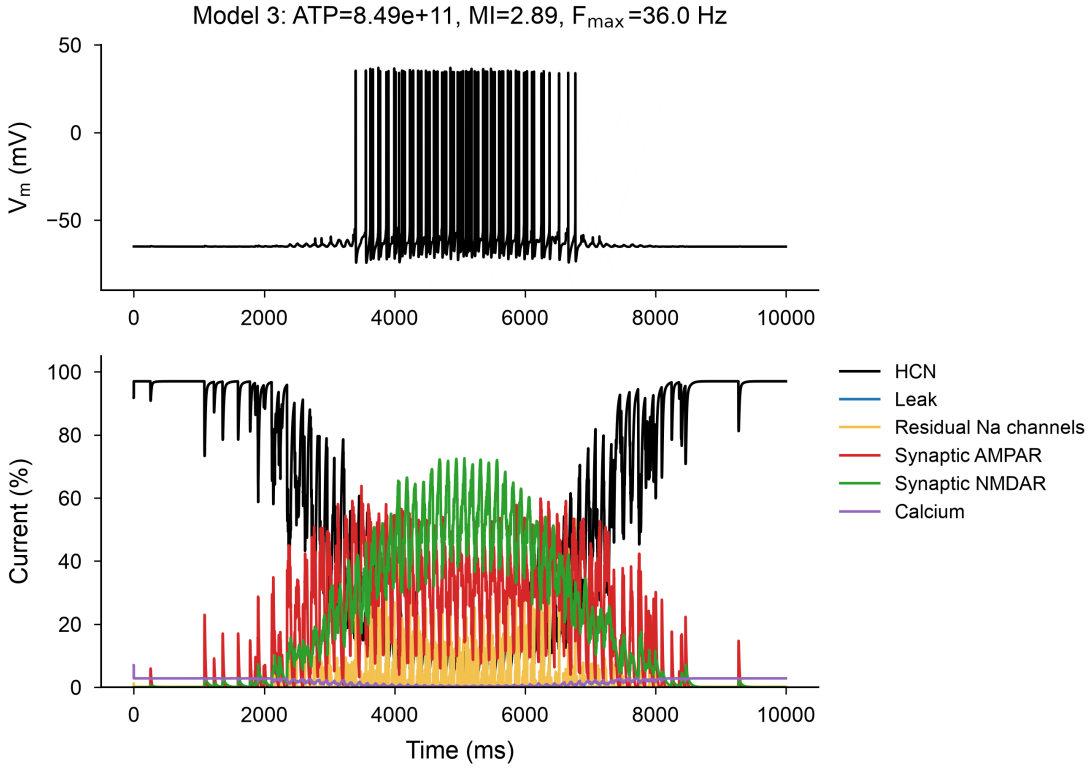
Model 3: ATP=8.49e+11, MI=2.89, F$_{max}$=36.0 Hz
V$_m$ (mV)
50
0
−50
0
2000
4000
6000
8000
10000
Current (%)
100
80
60
40
20
0
Time (ms)
HCN
Leak
Residual Na channels
Synaptic AMPAR
Synaptic NMDAR
Calcium

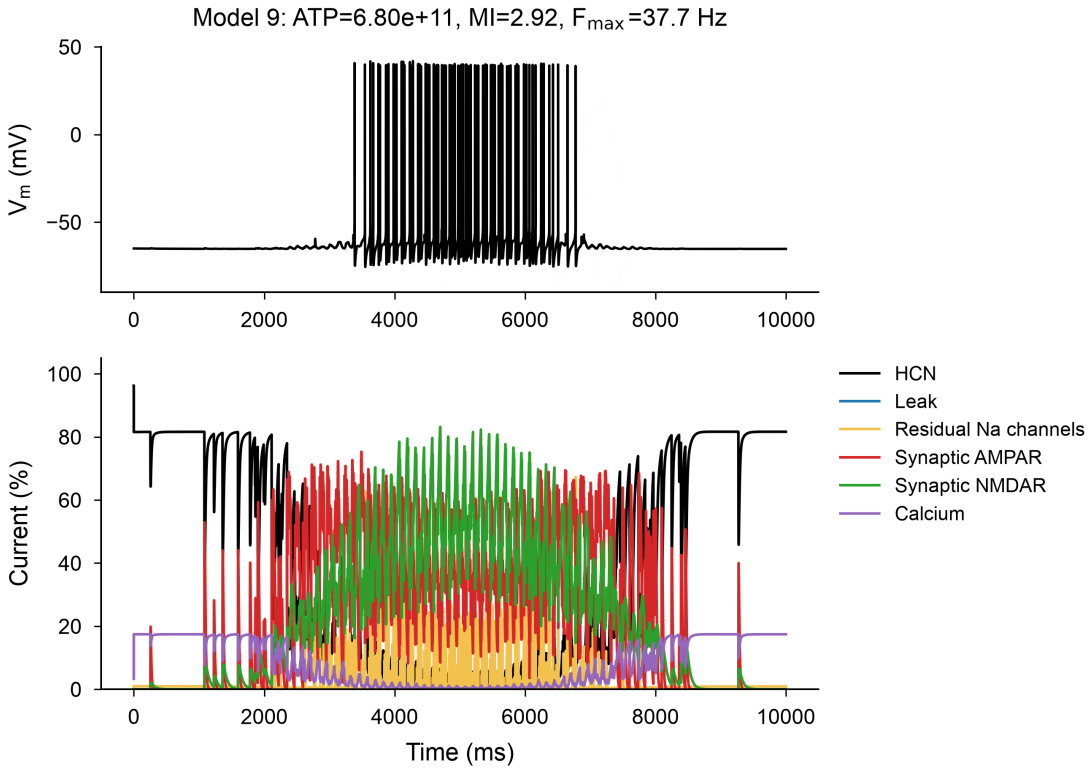
Model 9: ATP=6.80e+11, MI=2.92, F$_{max}$=37.7 Hz
V$_m$ (mV)
50
0
−50
0
2000
4000
6000
8000
10000
Current (%)
100
80
60
40
20
0
Time (ms)
HCN
Leak
Residual Na channels
Synaptic AMPAR
Synaptic NMDAR
Calcium

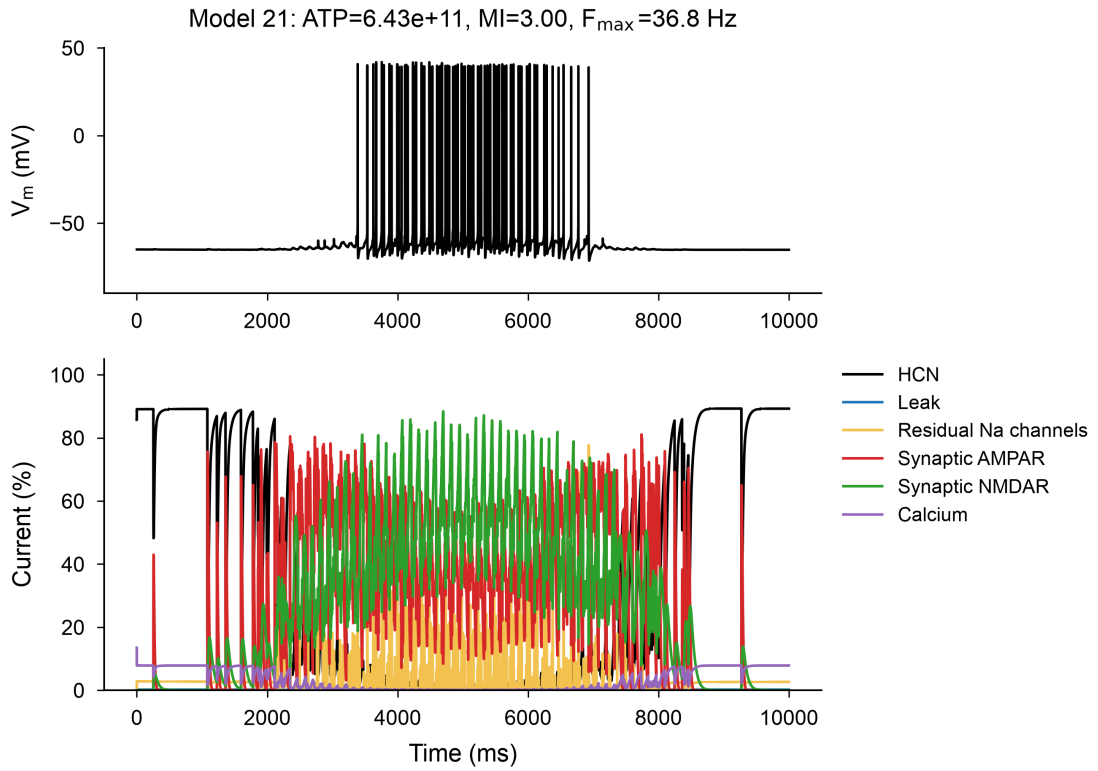

Figure 4.10 – 4.12 Temporal decomposition of currents for three representative models exhibiting similar functional outputs. Despite comparable firing behavior, models differ in the relative contributions of intrinsic and synaptic currents. This demonstrates that similar neuronal function can arise from distinct underlying mechanisms.

4.3 Information- and Energy-Theoretic Analysis

To assess the trade-off between place coding and energy consumption, we calculated the aggregated MI content and measured ATP usage via ion-counting during virtual place-field traversal. Thereby, we could quantify information and energy in our final population. The final models showed MI values within a moderate to close range (mean = 2.9 bits, SD = 0.19 bits), despite pronounced observed variation across parameters and current dynamics. This suggests that all models performed similarly during coding, possibly due to our tighter constraint on the shape of place fields. In comparison, ATP consumption varied more broadly (mean = $7.03e^{11}$ Moles of ATP, SD = $5.71e^{10}$ moles of ATP), indicating that similar levels of information transmission can be achieved at different energetic costs.

The weak global correlation between MI and ATP (r = 0.195) suggests these objectives are largely independent across the population, though this result should be

interpreted cautiously given the small sample size (n = 29) and likely limited statistical power. Similarly, while four models form a Pareto front consistent with an energy-information trade-off, this frontier is almost certainly incomplete and may not capture the full range of optimal solutions. Taken together, these findings offer tentative partial support for H1: Pareto-optimal trade-offs between spatial coding and energy efficiency exist in principle, but cannot be robustly characterized from the current population. Expanding the valid model population would be a necessary step before drawing stronger conclusions.

In contrast, MI exhibited a clearer positive correlation between peak firing rate (Fmax) and place-field width (FWHM; Table 4.2; Figures 4.14 - 4.15). Models with higher peak firing rates and a more pronounced place field width generally showed higher MI values. This indicates that information transmission directly depends on spiking activity. Surprisingly, ATP consumption showed only moderate correlations with firing rate (Figure 4.16). And an even weaker correlation with FWHM (Figure 4.17). The generally weaker correlation between ATP and place-field characteristics might explain the reduced correlation between ATP and MI.

One explanation is that distinct combinations of ion channels can produce similar place field properties. These can thereby produce similar MI content. However, they can differ substantially in their energetic cost. This may reflect differences in channel kinetics, activation threshold potentials, and ionic species transported. Taken together, these findings support the notion of ion channel degeneracy: while output firing properties tightly constrain information transfer, the energetic cost is not uniquely determined by these properties. Multiple ion channel configurations of varying metabolic cost can therefore converge on equivalent information encoding capacity.

Collectively, our results demonstrate that different parameter sets satisfy the same physiological constraints while relying on distinct underlying current compositions (i.e., degenerate). This reveals a many-to-one relationship between distinct sets of ion channel configurations and stable place coding.

Measurement	Value
MI	2.900 ± 0.190 bits
ATP consumption	7.03e+11 ± 5.71e+10
r(MI, ATP)	0.195
r(MI, F_{max})	0.891
r(MI, FWHM)	0.869
r(ATP, F_{max})	0.410
r(ATP, FWHM)	0.282

Table 4.2 Summary of mean values and standard deviations for information- and energy-related metrics, along with correlations with place field properties of the final population.

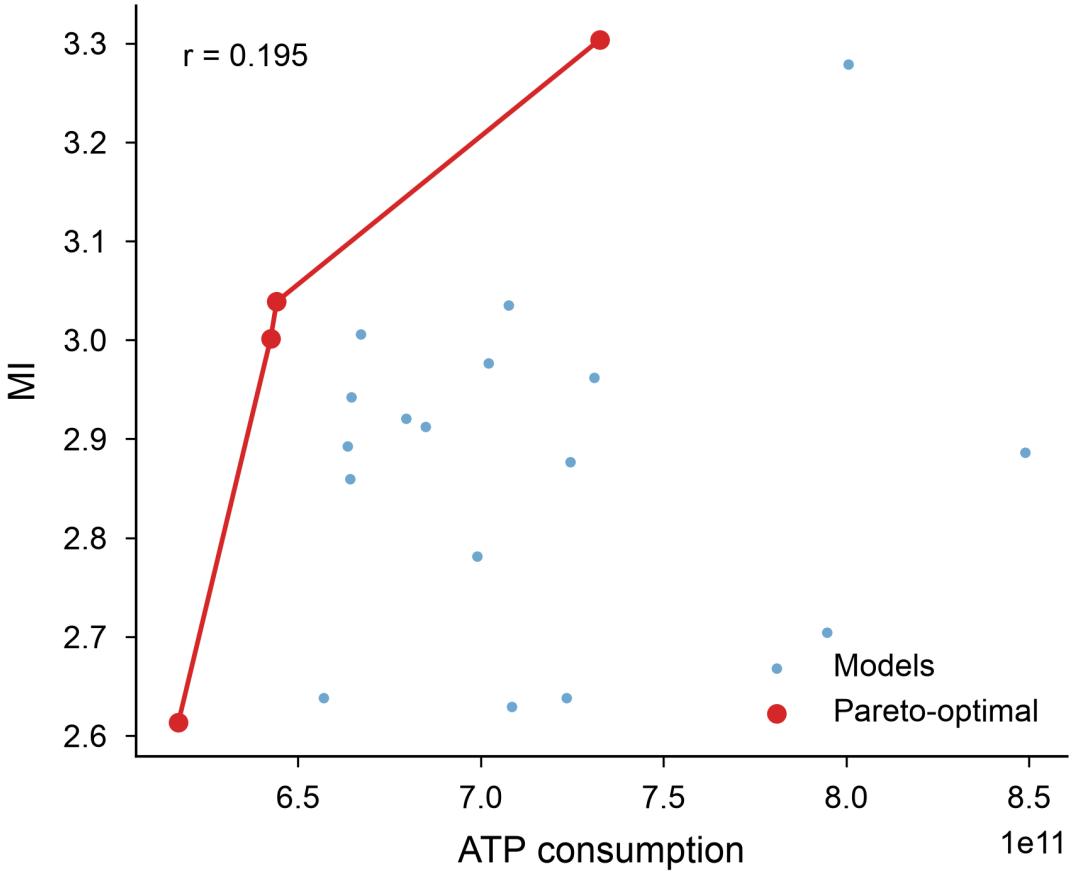

Figure 4.13 Scatter plot of mutual information (MI) versus adenosine triphosphate (ATP) in the valid model population with an emerging Pareto front.

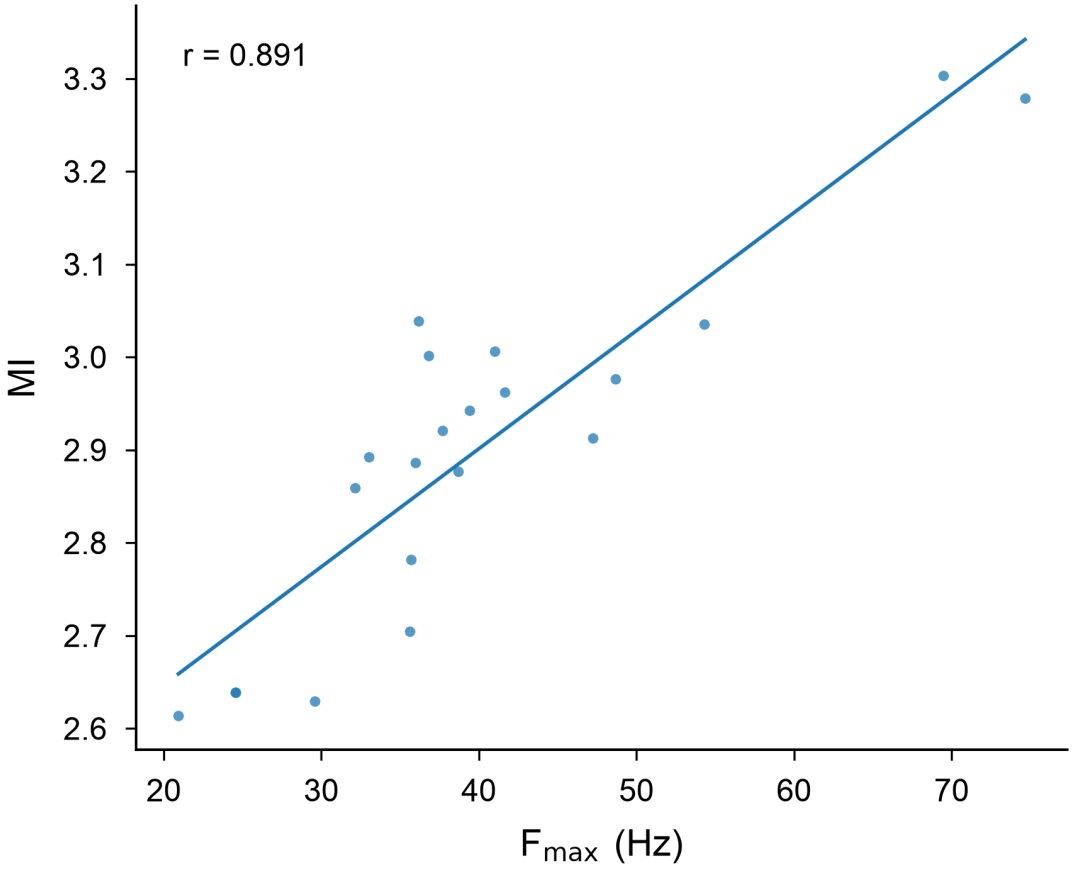

Figure 4.14 Scatter plot of mutual information (MI) versus maximum firing frequency (Fmax) during place-field traversal in the valid model population.

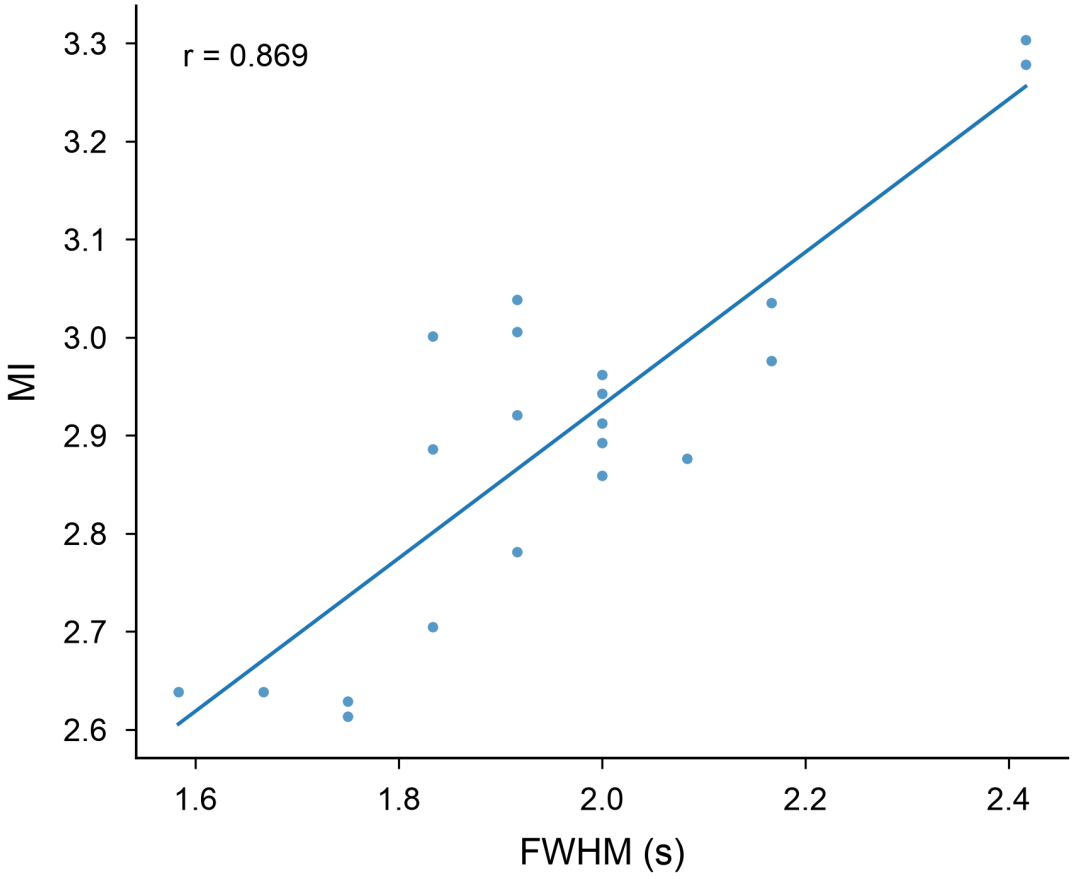

Figure 4.15 Scatter plot of mutual information (MI) versus full-width at half-maximum (FWHM) of the place-field in the valid model population.

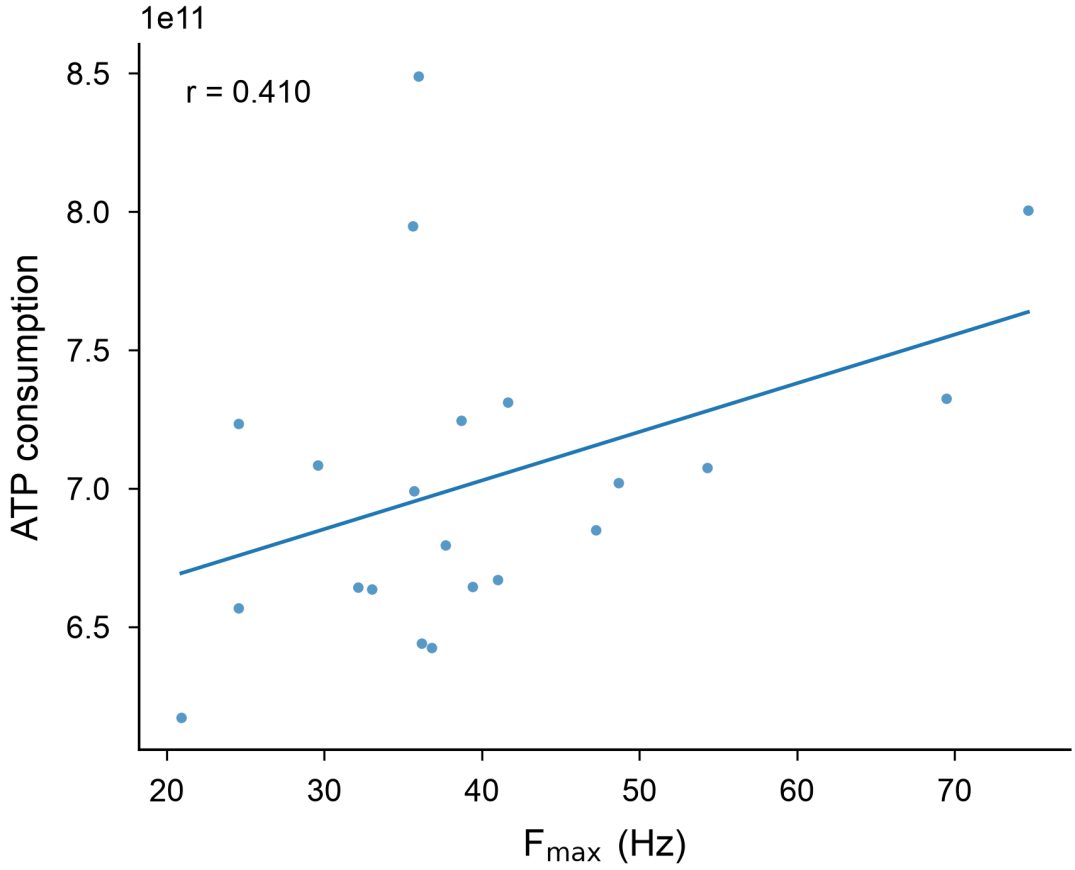

Figure 4.16 Scatter plot of adenosine triphosphate (ATP) use versus maximum firing frequency (Fmax) during place-field traversal in the valid model population.

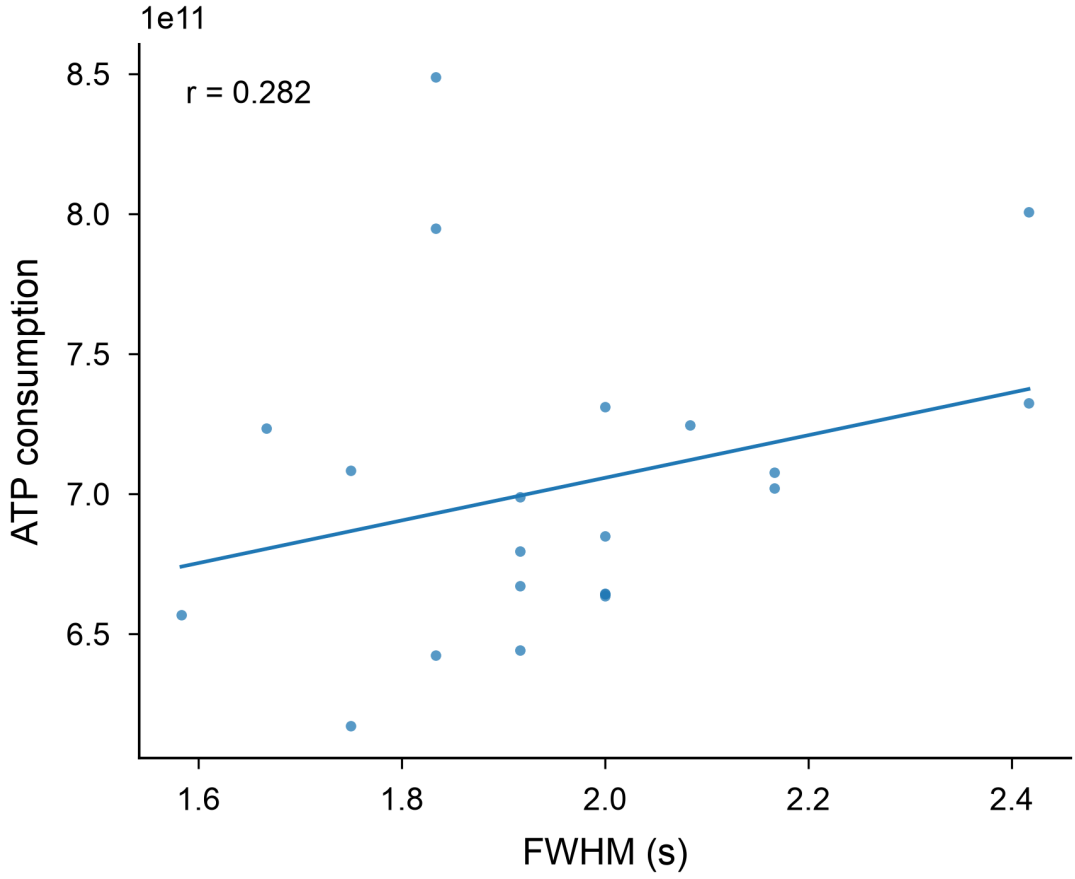

Figure 4.17 Scatter plot of adenosine triphosphate (ATP) use versus full-width at half-maximum (FWHM) of the place-field in the valid model population.

5 Discussion

Our findings show that stable place coding can be maintained across diverse parameter configurations, supporting the idea of ion-channel degeneracy as an underlying principle of neural function. This finding aligns with earlier research over the past decades showing that neurons, i.e., CA1 place cells, do not rely on a single solution in parameter space (Prinz et al., 2004; Rathour & Narayanan, 2014; Roy & Narayanan, 2021. Instead, neurons operate within a regime of multiple solutions that confer robustness to external perturbations (Goaillard et al., 2009; Goaillard & Marder, 2021). Although all our models produced similar electrophysiological and functional outcomes, their underlying current composition differed markedly. This dissociation between mechanism and function indicates that the same neuronal behavior can arise from different biophysical (i.e., ion-channel) implementations. However, contrary to our initial hypothesis, we didn't observe a marked trade-off between function and energy. This might be due to idiosyncrasies in

channel kinetics associated with different metabolic costs, which allow the relative independence of ATP consumption and place coding. These insights are crucial for interpreting experimental data, as similar recordings may reflect fundamentally different mechanisms.

5.1 Biophysical Interpretation

Our final population exhibited pronounced degeneracy in intrinsic parameters while converging on a similar functional output in place coding. This variability indicates that neuronal systems can maintain place-coding performance despite significant differences in their underlying biophysical mechanisms and energy efficiency. Moreover, we observed covariation among intrinsic parameters that exhibited antagonistic or agonistic behavior. This implies that some components of the neural substrate might be linked to others. However, this linkage might be the very reason neural systems are so robust to perturbations. If one component is perturbed, other mechanisms associated with the channel's specific function can compensate. Overall, our findings strongly support ion channel degeneracy as a fundamental principle of neural function. However, our idea that we can constrain ion channel degeneracy through evolutionarily informative trade-offs, such as the function-energy trade-off, that obey Pareto optimality, is only partially supported by our findings. There might be several reasons for this finding. For example, our constraints on the shape of the place field, in particular the place field width, might have been too strict, preventing heterogeneity in place coding that would have allowed a more pronounced trade-off. Another reason might be that there are competing objectives beyond energy and place coding that the population of models has been optimized for under the experimental constraints, and this might not show up in our functional space. Last, and most paradoxically, the optimization of place coding could have just gone hand in hand with the liberation of energy demands. And ion channel degeneracy might be the very reason this many-to-one relationship between energy and place coding is possible. However, the question of what constraints the energy demand would impose remains open.

5.2 Consequences for Cognitive Science

Degeneracy might be relevant not only to ion channels in the brain. It is plausible that degeneracy operates across multiple scales, from subcellular mechanisms to network functions and even cognitive faculties. For example, there are different ways to solve a task one is ruminating about or to navigate a new city one has never been to before. One solution does not necessarily exclude other possibilities. Instead, many different approaches might be found for a specific problem. Moreover, earlier work by Uri Alon and others suggests that evolutionary trade-offs might be ubiquitous and obey optimality principles such as the Pareto law. Degeneracy could be a mechanism for using different substrates provided by nature to achieve a similar functional outcome. Even more, degeneracy must logically follow from the principle of evolution, that is, the dynamic accumulation of random changes in DNA that introduce new genetic variation. Thus, degeneracy might be seen as a prerequisite for evolutionary changes. Del Giudice and Crespi defined the dominant objectives that every cognitive system, whether natural or artificial, must fulfill: performance, robustness, efficiency, and flexibility. However, trade-offs are necessary to mediate between these seemingly conflicting demands. To design a successful cognitive system, it is necessary to account for these trade-offs. Hence, it is tempting to speculate that degeneracy and cognition might be closely related. Therefore, ion channel degeneracy is only one of many ways to achieve this, and more may be discovered in the future.

5.3 Implications for Modeling and Experiments

Degeneracy questions the idea that parameters in conductance-based models are uniquely identifiable. Instead, it indicates that model fitting should aim to find a range of solutions rather than a single optimal model. For experimental research, this suggests that relying solely on functional measurements makes it difficult to pinpoint specific mechanisms. To clarify the underlying processes, additional constraints or targeted perturbations might be necessary. In our case, we tried to achieve this by constraining the parameter space with evolutionary-informed constraints on place coding and energy consumption. Although ion channel degeneracy couldn’t be explained by this trade-off, other trade-offs among functions and objectives might exist that effectively reduce the high-dimensional parameter space of degenerative neurons to lower-dimensional manifolds.

5.4 Limitations and Future Directions

Several limitations should be acknowledged. The initial strict place-field criteria produced a highly restricted, relatively uniform population. This limited variability may mask relationships between place coding and metabolic costs, so we also examined a more relaxed subset of place fields to capture a wider range of phenotypes. Even with the relaxed criteria, information content remained consistently constrained across models, indicating that intrinsic conductance variability does not strongly influence spatial information encoding. Consequently, the weak MI–ATP relationship might stem from inherent constraints in place-field encoding rather than from overly restrictive filtering. Due to computational constraints, only one traversal per model was simulated, and mutual information was estimated using a single-trial spatial information metric based on firing-rate profiles, rather than from trial-based responses. Relaxing the peak firing rate constraint increased the number of valid models but did not significantly expand the information value distribution. Across models, information was strongly correlated with peak firing rate ($r = 0.89$) and place-field width ($r = 0.87$), but only weakly with ATP consumption ($r = 0.195$). This indicates that, within the tested parameter space, spatial information depends primarily on place-field shape rather than on metabolic cost. The information content in place cells is largely driven by firing dynamics (rate and width). At the same time, metabolic cost varies more independently and is not a major factor constraining information encoding in our model population.

Future work could explore how a more diverse set of place-field shapes affects the trade-off between MI and ATP consumption. We cannot rule out that our place-field constraint was obscuring a significant MI-ATP relationship. However, there are also alternative explanations for the weak relationship between our objectives. There might have been competing objectives we have not accounted for, that would have further constrained our degenerant parameter space. Another possibility is that there is truly no function-energy trade-off in CA1 place cells. Moreover, other cell types and their functions can be considered when examining evolutionarily informed energy-function trade-offs. The pyramidal cell in the hippocampus is only one of many cell types that might have been tightly optimized for spatial coding. Therefore, this might be why they have not been amenable to our experimental approach. Lastly, a more detailed analysis of the contributions of underlying ion-channel conductances, combined with a virtual-

knockout approach for individual channels, could reveal the specific effects of these channels on place coding and energy consumption.

6 Conclusion

In summary, this study shows that neuronal function can result from various parameter configurations and mechanisms. This many-to-one relationship between parameters and function emphasizes degeneracy as a key organizing principle in neuronal systems.

7 Literature

Alonso, L. M., & Marder, E. (2019). Visualization of currents in neural models with similar behavior and different conductance densities. *eLife*, *8*, e42722. https://doi.org/10.7554/eLife.42722

Basak, R., & Narayanan, R. (2018). Spatially dispersed synapses yield sharply-tuned place cell responses through dendritic spike initiation. *The Journal of Physiology*, *596*(17), 4173–4205. https://doi.org/10.1113/JP275310

Basak, R., & Narayanan, R. (2020). Robust emergence of sharply tuned place-cell responses in hippocampal neurons with structural and biophysical heterogeneities. *Brain Structure and Function*, *225*(2), 567–590. https://doi.org/10.1007/s00429-019-02018-0

Bean, B. P. (2007). The action potential in mammalian central neurons. *Nature Reviews Neuroscience*, *8*(6), 451–465. https://doi.org/10.1038/nrn2148

Bird, A. D., Cuntz, H., & Jedlicka, P. (2022). *Robust and consistent measures of pattern separation based on information theory and demonstrated in the dentate gyrus* [Preprint]. Neuroscience. https://doi.org/10.1101/2022.11.04.515143

Carnevale, N. T., & Hines, M. L. (2006). *The NEURON Book* (1st ed.). Cambridge University Press. https://doi.org/10.1017/CBO9780511541612

Damasio, A. R. (1989). The Brain Binds Entities and Events by Multiregional Activation from Convergence Zones. *Neural Computation*, *1*(1), 123–132. https://doi.org/10.1162/neco.1989.1.1.123

Dehaene, S. (2001). Towards a cognitive neuroscience of consciousness: Basic evidence and a workspace framework. *Cognition*, *79*(1–2), 1–37. https://doi.org/10.1016/S0010-0277(00)00123-2

Del Giudice, M., & Crespi, B. J. (2018). Basic functional trade-offs in cognition: An integrative framework. *Cognition*, *179*, 56–70. https://doi.org/10.1016/j.cognition.2018.06.008

Edelman, G. M., & Gally, J. A. (2001). Degeneracy and complexity in biological systems. *Proceedings of the National Academy of Sciences*, *98*(24), 13763–13768. https://doi.org/10.1073/pnas.231499798

Engel, A. K., Fries, P., & Singer, W. (2001). Dynamic predictions: Oscillations and synchrony in top–down processing. *Nature Reviews Neuroscience*, *2*(10), 704–716. https://doi.org/10.1038/35094565

Galow, L. V., Schneider, J., Lewen, A., Ta, T.-T., Papageorgiou, I. E., & Kann, O. (2014). Energy substrates that fuel fast neuronal network oscillations. *Frontiers in Neuroscience*, *8*. https://doi.org/10.3389/fnins.2014.00398

Goaillard, J.-M., & Marder, E. (2021). Ion Channel Degeneracy, Variability, and Covariation in Neuron and Circuit Resilience. *Annual Review of Neuroscience*, *44*(1), 335–357. https://doi.org/10.1146/annurev-neuro-092920-121538

Goaillard, J.-M., Taylor, A. L., Schulz, D. J., & Marder, E. (2009). Functional consequences of animal-to-animal variation in circuit parameters. *Nature Neuroscience*, *12*(11), 1424–1430. https://doi.org/10.1038/nn.2404

Grienberger, C., Milstein, A. D., Bittner, K. C., Romani, S., & Magee, J. C. (2017). Inhibitory suppression of heterogeneously tuned excitation enhances spatial coding in CA1 place cells. *Nature Neuroscience*, *20*(3), 417–426. https://doi.org/10.1038/nn.4486

Harris, J. J., Engl, E., Attwell, D., & Jolivet, R. B. (2019). Energy-efficient information transfer at thalamocortical synapses. *PLOS Computational Biology*, *15*(8), e1007226. https://doi.org/10.1371/journal.pcbi.1007226

Harris, J. J., Jolivet, R., Engl, E., & Attwell, D. (2015). Energy-Efficient Information Transfer by Visual Pathway Synapses. *Current Biology*, *25*(24), 3151–3160. https://doi.org/10.1016/j.cub.2015.10.063

Hines, M. L., & Carnevale, N. T. (1997). The NEURON Simulation Environment. *Neural Computation*, *9*(6), 1179–1209. https://doi.org/10.1162/neco.1997.9.6.1179

Jain, A., & Narayanan, R. (2020). Degeneracy in the emergence of spike-triggered average of hippocampal pyramidal neurons. *Scientific Reports*, *10*(1), 374. https://doi.org/10.1038/s41598-019-57243-8

Jedlicka, P., Bird, A. D., & Cuntz, H. (2022). Pareto optimality, economy–effectiveness trade-offs and ion channel degeneracy: Improving population modelling for single neurons. *Open Biology*, *12*(7), 220073. https://doi.org/10.1098/rsob.220073

Marder, E. (2012). Neuromodulation of Neuronal Circuits: Back to the Future. *Neuron*, *76*(1), 1–11. https://doi.org/10.1016/j.neuron.2012.09.010

Marder, E., & Bucher, D. (2007). Understanding Circuit Dynamics Using the Stomatogastric Nervous System of Lobsters and Crabs. *Annual Review of Physiology*, *69*(1), 291–316. https://doi.org/10.1146/annurev.physiol.69.031905.161516

Marder, E., & Calabrese, R. L. (1996). Principles of rhythmic motor pattern generation. *Physiological Reviews*, *76*(3), 687–717. https://doi.org/10.1152/physrev.1996.76.3.687

Marder, E., & Goaillard, J.-M. (2006). Variability, compensation and homeostasis in neuron and network function. *Nature Reviews Neuroscience*, *7*(7), 563–574. https://doi.org/10.1038/nrn1949

Mertens, E. J., Leibner, Y., Pie, J., Galakhova, A. A., Waleboer, F., Meijer, J., Heistek, T. S., Wilbers, R., Heyer, D., Goriounova, N. A., Idema, S., Verhoog, M. B., Kalmbach, B. E., Lee, B. R., Gwinn, R. P., Lein, E. S., Aronica, E., Ting, J., Mansvelder, H. D., … De

Kock, C. P. J. (2024). Morpho-electric diversity of human hippocampal CA1 pyramidal neurons. *Cell Reports*, *43*(4), 114100. https://doi.org/10.1016/j.celrep.2024.114100

Migliore, R., Lupascu, C. A., Bologna, L. L., Romani, A., Courcol, J.-D., Antonel, S., Van Geit, W. A. H., Thomson, A. M., Mercer, A., Lange, S., Falck, J., Rössert, C. A., Shi, Y., Hagens, O., Pezzoli, M., Freund, T. F., Kali, S., Muller, E. B., Schürmann, F., … Migliore, M. (2018). The physiological variability of channel density in hippocampal CA1 pyramidal cells and interneurons explored using a unified data-driven modeling workflow. *PLOS Computational Biology*, *14*(9), e1006423. https://doi.org/10.1371/journal.pcbi.1006423

Mittal, D., & Narayanan, R. (2022). Heterogeneous stochastic bifurcations explain intrinsic oscillatory patterns in entorhinal cortical stellate cells. *Proceedings of the National Academy of Sciences*, *119*(52), e2202962119. https://doi.org/10.1073/pnas.2202962119

Montgomery, N., & Wehr, M. (2010). Auditory Cortical Neurons Convey Maximal Stimulus-Specific Information at Their Best Frequency. *The Journal of Neuroscience*, *30*(40), 13362–13366. https://doi.org/10.1523/JNEUROSCI.2899-10.2010

Moser, E. I., Moser, M.-B., & McNaughton, B. L. (2017). Spatial representation in the hippocampal formation: A history. *Nature Neuroscience*, *20*(11), 1448–1464. https://doi.org/10.1038/nn.4653

Moujahid, A., d'Anjou, A., Torrealdea, F. J., & Torrealdea, F. (2011). Energy and information in Hodgkin-Huxley neurons. *Physical Review E*, *83*(3), 031912. https://doi.org/10.1103/PhysRevE.83.031912

O'Hare, J. K., Wang, J., Shala, M. D., Polleux, F., & Losonczy, A. (2024a). *Distal tuft dendrites shape and maintain new place fields* [Preprint]. Neuroscience. https://doi.org/10.1101/2024.02.26.582144

O'Hare, J. K., Wang, J., Shala, M. D., Polleux, F., & Losonczy, A. (2024b). *Variable recruitment of distal tuft dendrites shapes new hippocampal place fields*. https://doi.org/10.1101/2024.02.26.582144

O'Keefe, J. (1976). Place units in the hippocampus of the freely moving rat. *Experimental Neurology*, *51*(1), 78–109. https://doi.org/10.1016/0014-4886(76)90055-8

Pareto, V. (2014). *Manual of political economy: A critical and variorum edition* (A. Montesano, A. Zanni, L. Bruni, J. S. Chipman, & M. McLure, Eds.; First edition). Oxford University Press.

Prinz, A. A., Bucher, D., & Marder, E. (2004). Similar network activity from disparate circuit parameters. *Nature Neuroscience*, *7*(12), 1345–1352. https://doi.org/10.1038/nn1352

Rathour, R. K., & Narayanan, R. (2014). Homeostasis of functional maps in active dendrites emerges in the absence of individual channelostasis. *Proceedings of the National Academy of Sciences*, *111*(17). https://doi.org/10.1073/pnas.1316599111

Roy, A., & Narayanan, R. (2021). Spatial information transfer in hippocampal place cells depends on trial-to-trial variability, symmetry of place-field firing, and biophysical heterogeneities. *Neural Networks*, *142*, 636–660. https://doi.org/10.1016/j.neunet.2021.07.026

Seenivasan, P., & Narayanan, R. (2020a). Efficient phase coding in hippocampal place cells. *Physical Review Research*, *2*(3), 033393. https://doi.org/10.1103/PhysRevResearch.2.033393

Seenivasan, P., & Narayanan, R. (2020b). Efficient phase coding in hippocampal place cells. *Physical Review Research*, *2*(3), 033393. https://doi.org/10.1103/PhysRevResearch.2.033393

Shoval, O., Sheftel, H., Shinar, G., Hart, Y., Ramote, O., Mayo, A., Dekel, E., Kavanagh, K., & Alon, U. (2012). Evolutionary Trade-Offs, Pareto Optimality, and the Geometry of Phenotype Space. *Science*, *336*(6085), 1157–1160. https://doi.org/10.1126/science.1217405

Singer, W., & Gray, C. M. (1995). Visual Feature Integration and the Temporal Correlation Hypothesis. *Annual Review of Neuroscience*, *18*(1), 555–586. https://doi.org/10.1146/annurev.ne.18.030195.003011

Souza, B. C., & Tort, A. B. L. (2017). Asymmetry of the temporal code for space by hippocampal place cells. *Scientific Reports*, *7*(1), 8507. https://doi.org/10.1038/s41598-017-08609-3

Stöber, T. M., Batulin, D., Triesch, J., Narayanan, R., & Jedlicka, P. (2023). Degeneracy in epilepsy: Multiple routes to hyperexcitable brain circuits and their repair. *Communications Biology*, *6*(1), 479. https://doi.org/10.1038/s42003-023-04823-0

Swensen, A. M., & Bean, B. P. (2005). Robustness of Burst Firing in Dissociated Purkinje Neurons with Acute or Long-Term Reductions in Sodium Conductance. *The Journal of Neuroscience*, *25*(14), 3509–3520. https://doi.org/10.1523/JNEUROSCI.3929-04.2005

Szekely, P., Sheftel, H., Mayo, A., & Alon, U. (2013). Evolutionary Tradeoffs between Economy and Effectiveness in Biological Homeostasis Systems. *PLoS Computational Biology*, *9*(8), e1003163. https://doi.org/10.1371/journal.pcbi.1003163

Timme, N. M., & Lapish, C. (2018). A Tutorial for Information Theory in Neuroscience. *Eneuro*, *5*(3), ENEURO.0052-18.2018. https://doi.org/10.1523/ENEURO.0052-18.2018

Tkacˇik, G. (2025). *Information Processing in Biochemical Networks*.

Tononi, G., Boly, M., Massimini, M., & Koch, C. (2016). Integrated information theory: From consciousness to its physical substrate. *Nature Reviews Neuroscience*, *17*(7), 450–461. https://doi.org/10.1038/nrn.2016.44

Von Der Malsburg, C. (1994). The Correlation Theory of Brain Function. In E. Domany, J. L. Van Hemmen, & K. Schulten (Eds.), *Models of Neural Networks* (pp. 95–119). Springer New York. https://doi.org/10.1007/978-1-4612-4320-5_2

Yamada-Hanff, J., & Bean, B. P. (2013). Persistent Sodium Current Drives Conditional Pacemaking in CA1 Pyramidal Neurons under Muscarinic Stimulation. *The Journal of Neuroscience*, *33*(38), 15011–15021. https://doi.org/10.1523/JNEUROSCI.0577-13.2013

8 Appendix

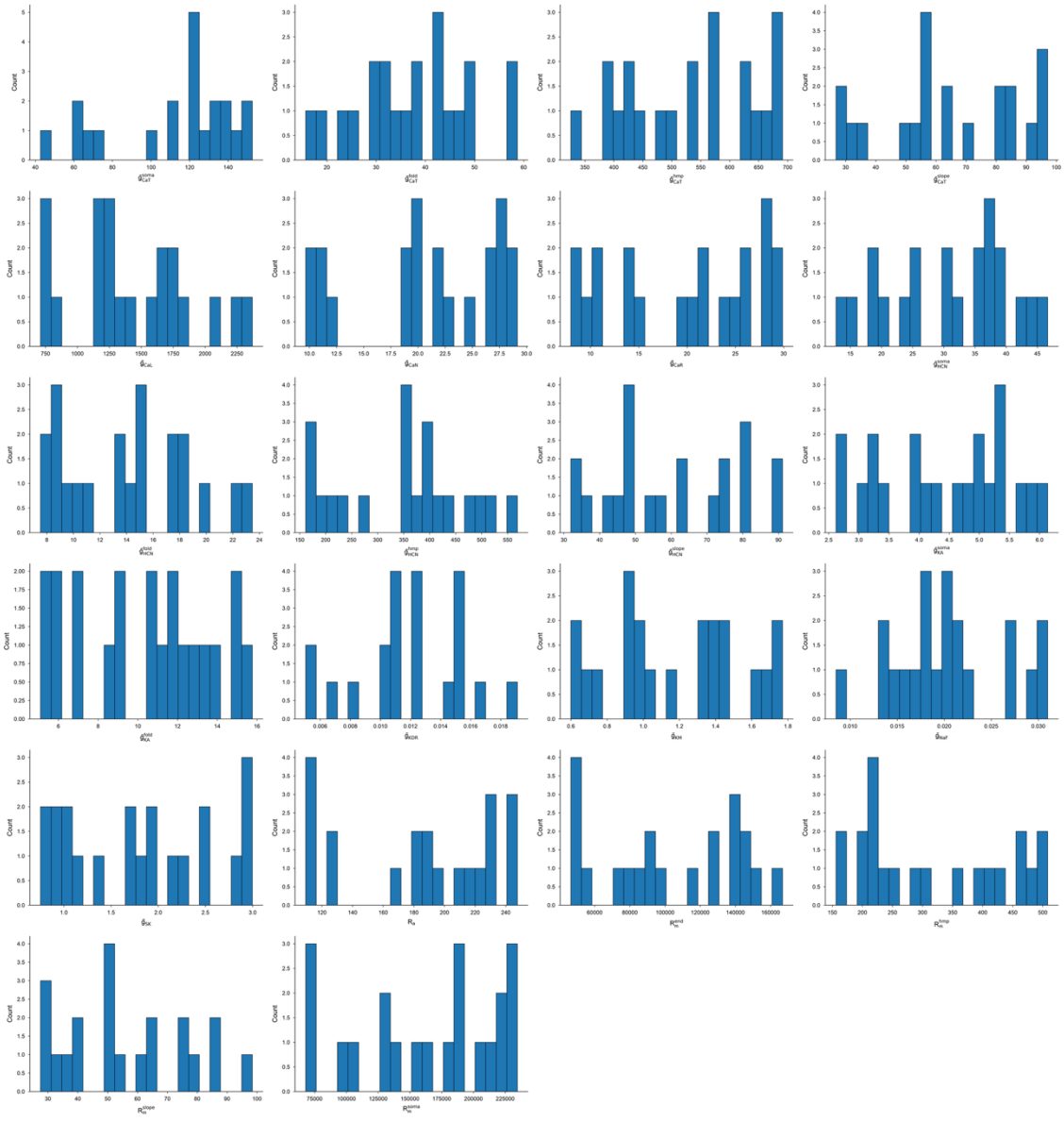

Figure S1 Parameter distributions across the valid model population.

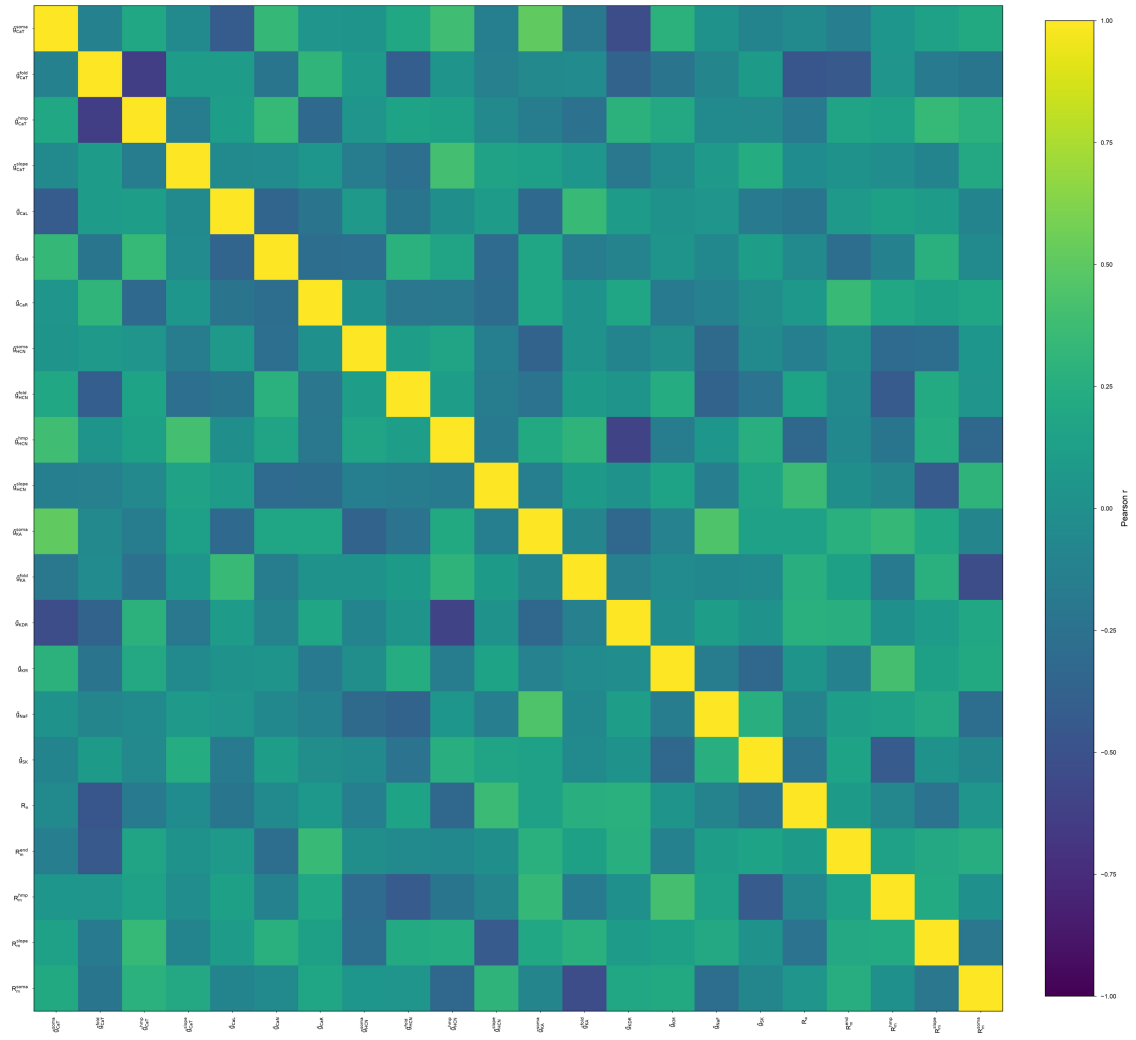

Figure S2 Confusion matrix among all possible parameter combinations.